Water vapor anomaly over the tropical western Pacific in El Niño winters from radiosonde and satellite observations and ERA5 reanalysis data

Minkang Du[1,2,3]   Kaiming Huang[1,2,3]   Shaodong Zhang[1,2]   Chunming Huang[1,2]

Yun Gong[1,2]   and   Fan Yi[1,2,3]

[1]School of Electronic Information, Wuhan University, Wuhan, China

[2]Key Laboratory of Geospace Environment and Geodesy, Ministry of Education, Wuhan, China

[3]State Observatory for Atmospheric Remote Sensing, Wuhan, China

Correspondence: Kai Ming Huang (hkm@whu.edu.cn)

Abstract. Using radiosonde observations at five stations in the tropical western Pacific and reanalysis data for 15 years from 2005 to 2019, we report an extremely negative anomaly in atmospheric water vapor during the super El Niño winter of 2015/16, and compare the anomaly with that in the other three El Niño winters. Strong specific humidity anomaly is concentrated below 8 km of the troposphere with a peak at 2.5-3.5 km, and column integrated water vapor mass anomaly over the five radiosonde sites has a large negative correlation coefficient of -0.63 with oceanic Niño3.4 index, but with a lag of about 2-3 months. In general, the tropical circulation anomaly in the El Niño winter is characterized by divergence (convergence) in the lower troposphere over the tropical western (eastern) Pacific, thus the water vapor decreases over the tropical western Pacific as upward motion is suppressed. The variability of the Hadley circulation is quite small and has little influence on the observed water vapor anomaly. The anomaly of the Walker circulation makes a considerable contribution to the total anomaly in all the four El Niño winters, especially in the 2006/07 and 2015/16 eastern-Pacific (EP) El Niño events. The monsoon circulation shows a remarkable change from one event to another, and its anomaly is large in the 2009/10 and 2018/19 central-Pacific (CP) El Niño winters and small in the two EP El Niño winters. The observed water vapor anomaly is caused mainly by the Walker circulation anomaly in the super EP event of 2015/16 but by the monsoon circulation anomaly in the strong CP event of 2009/10. The roles of the Hadley, Walker and monsoon circulations in the EP and CP events are confirmed by the composite EP and CP El Niños based on the reanalysis data for 41 years. Owing to the anomalous decrease in upward transport of water vapor during the El Niño winter, lower cloud amounts and more outgoing longwave radiation over the five stations are clearly presented in satellite observation. In addition, a detailed comparison of water vapor in the reanalysis, radiosonde and satellite data shows a fine confidence level of the datasets, nevertheless, the reanalysis seems to slightly underestimate the water vapor over the five stations in the 2009/10 winter.

1 Introduction

As a dominant greenhouse gas in the atmosphere, water vapor has a profound impact on global energy budgets not only through latent heat release upon phase transitions (Held and Soden, 2000), but also through cloud formation that reflects long-wave radiation from below and short-wave radiation from above (Stevens et al., 2017), thus water vapor plays a substantial role in the formation and evolution of the climate system. The tropical Pacific is a major convection center and a region with abundant water vapor. Sea surface temperature (SST) anomalies in the tropical Pacific has an important influence on water vapor transport, cloud cover and precipitation distribution due to the tropical circulation changes caused by El Niño-Southern Oscillation (ENSO). ENSO is characterized by anomalous SST in the tropical Pacific. During ENSO, there is significant precipitation variability in the Euro-Mediterranean (López-Parages and Rodríguez-Fonseca, 2012), Middle East (Sandeep and Ajayamohan, 2018), southwest central Asia (Mariotti, 2007), western Africa (Okazaki et al., 2015), Pacific Ocean (Quartly et al., 2000) and continental USA (Lee et al., 2014). ENSO has an effect on seasonal rainfall in East Asian by inducing a weaker and later onset of the Indian monsoon circulation (Dai and Wigley, 2000; Zhao et al., 2010; Yan et al., 2018). Vertical cloud anomalies in the tropical Atlantic from Aqua Moderate Resolution Imaging Spectroradiometer are linked to ENSO-induced shift and weakening of the Walker circulation and Hadley cell near the equator (Madenach et al., 2019). The strong 1997/98 El Niño resulted in cloud structure anomalies and their radiative property changes over the tropical Pacific (Sun et al., 2012), and increased upper tropospheric cirrus over the mid-Pacific but decreased cirrus over Indonesia (Massie et al., 2000). Numerical investigation also indicated that warm water volume transport and precipitation change are associated with ENSO (Ishida et al., 2008; Hill et al., 2009).

El Niño is generally classified into central-Pacific (CP) El Niño, also known as El Niño Modoki, and

eastern-Pacific (EP) El Niño based on distinct spatial distributions of warming SST anomaly averaged

over the Niño4 and Niño3 regions (Ashok et al., 2007; Yu and Kao, 2009; Yeh et al., 2009), respectively.

The 2006/07 and 2015/16 events are the EP El Niño because of the stronger SST anomaly during the

boreal winter (December to February, as DJF) in the Niño3 region than in the Niño4 region, while

correspondingly, the 2009/10 and 2018/19 events are categorized as the CP El Niño (Yeh et al., 2009).

The two types of El Niño have different effects on precipitation, surface temperature, moisture transport

and carbon cycle over many parts of the world (Weng et al., 2008; Kug et al., 2009; Wang et al., 2013;

Yeh et al., 2014; Gu and Adler, 2016; Wang et al., 2018). Su and Jiang (2013) and Takahashi et al. (2013)

suggested that water vapor anomaly over the tropical ocean is mainly controlled by thermodynamic

process during the 2006/07 EP El Niño, but by both dynamic and thermodynamic processes during the

2009/10 CP El Niño.

The EP El Niño in 2015/16 winter is one of the strongest ENSO events on record. Compared to the

strong 1982/83 and 1997/98 El Niños, the 2015/16 El Niño shows distinct aspects that the largest SST

anomalies are extended toward the central Pacific (Paek et al., 2017; L'Heureux et al., 2017). As the

unusual characteristics, the global effects of the 2015/16 event have attracted much attention. Palmeiro et

al. (2017) proposed that an early stratospheric final warming over the polar region and anomalous

precipitation over southern Europe in 2016 were related to the 2015/16 super El Niño. Li et al. (2018)

revealed that the combined effect of the 2015 ENSO warm phase and Madden-Julian Oscillation

(MJO)-4 index negative phase caused a significant deficit of precipitation on the Canadian Prairies in

May and June 2015. A striking freshwater anomaly was observed in the equatorial Pacific during the

onset of 2015/16 event (Gasparin and Roemmich, 2016), and rainfall $\delta^{18}O$ in the southern Papua was

generally enriched by 1.6‰–2‰ during the 2015 El Niño than during the 2013/14 ENSO-normal period

(Permana et al., 2016). Owing to convection anomaly during the 2015/16 El Niño, water vapor in the

tropical lower stratosphere was increased by hydration of the lower stratosphere through convectively

detrained cloud ice (Avery et al., 2017), and quasi-biennial oscillation in the tropical stratospheric wind

was disrupted because of dramatic relocation of deep convection (Dunkerton, 2016; Newman et al.,

2016). Hence, the 2015/16 El Niño had important influences on the circulation and composition transport

and the mass exchange between the troposphere and stratosphere. In this paper, we investigate water

vapor anomaly over the tropical western Pacific in the CP and EP El Niño events from radiosonde and

satellite observations, in particular, extreme anomaly in the 2015/16 super El Niño winter, and explore

the contributions of the tropical Hadley, Walker and monsoon circulation changes to the observed water

vapor anomalies in the different El Niño events.

The data used are briefly described in section 2. In section 3, water vapor anomalies in four El Niño

winters are presented, and the relationship between the ENSO intensity and the water vapor anomaly at

the observational stations is explored. In section 4, we decompose the tropical circulation into the Hadley,

Walker and monsoon circulation components, and estimate the roles of these circulations in the water

vapor variation. Tropical cloud and outgoing longwave radiation (OLR) are investigated in section 5. A

discussion of the water vapor data quality is provided in section 6. Finally, we summarize the results in

section 7.

2. Data

In present study, we investigate the atmospheric water vapor by using radiosonde observations at five

tropical stations for 15 years from January 2005 to December 2019, which are provided by the national

oceanic   and   atmosphere   administration   (NOAA)   at   the   website   of

108 The five radiosonde stations are at Koror (7.33°N,

109 134.48°E), Yap (9.48°N, 138.08°E), Guam (13.55°N, 144.83°E), Truk (7.47°N, 151.85°E) and Ponape

110 (6.97°N, 158.22°E), located in the western Pacific warm pool. Balloon was launched twice daily at 0000

111 UT and 1200 UT, and during balloon ascent, sensing payload on balloon can obtain many meteorological

112 parameters, such as atmospheric pressure, temperature, relative humidity, and wind speed and direction.

113 We plot daily temperature, relative humidity, and wind speed time series observed by radiosonde to

114 identify potential outliers, and then the high resistant asymmetric biweight technique is applied to weed

115 out the outliers (Lanzante, 1996). The outlier data are very few, and the outliers of temperature, wind and

116 relative humidity account for only 0.09%, 0.08% and 0.02% of all observational data at the five stations

117 during 15 years, respectively. The radiosonde data is linearly interpolated to a vertical grid of 50 m, and

118 the interpolated data below 10 km is utilized to analyze the atmospheric water vapor variation. Burst

119 height of balloon is usually more than 30 km, thus the data availability below 10 km is high. In the period

120 that we focus on, the data are missing for about 4, 2, 1 and 4 months over Yap, Guam, Truk and Ponape,

121 respectively, and they are almost entirely from the several continuous observational missing rather than

122 balloon burst below 10 km.

123 Specific humidity can be derived from the profile of meteorological parameters observed by

124 radiosonde. The saturated vapor pressure e_s is calculated according to a modified version of the

125 Magnus formula as follows (Murray, 1967),

126 $$e_s = 6.1078 \times \exp\left[\frac{17.269\left(T - 273.16\right)}{T - 35.86}\right] \tag{1}$$

127 where T is the temperature in units of K. And then, the specific humidity q (g kg^{-1}) is determined

128 from the following equations,

$$e = RH \times e_s \tag{2}$$

129

$$q = \frac{0.622e}{p - 0.378e} \tag{3}$$

130

131 where e is the vapor pressure; RH is the relative humidity; and p is the pressure with units of hPa.

132 In addition, we use the monthly specific humidity, horizontal winds from surface to 300 hPa during

133 the period of 2005-2019, obtained from the European centre for medium-range weather forecasts

134 (ECMWF) ERA5 reanalysis data, to investigate the water vapor anomaly and tropical atmospheric

135 circulation in the region of the radiosonde stations. The reanalysis data is produced by a sequential 4D

136 variational data assimilation scheme, with a latitudinal and longitudinal resolution of $0.25° \times 0.25°$ at 37

137 pressure levels from 1000 to 1 hPa (Hersbach et al., 2020). The data is available at the website of

138 https://cds.climate.copernicus.eu/cdsapp#!/home/.

139 To assess the atmospheric water vapor as compare to the reanalysis data and the radiosonde

140 observations, a further evaluation is carried out using Aqua atmospheric infrared sounder (AIRS) water

141 vapor mass mixing ratio data from 2005-2019. AIRS is a hyperspectral infrared spectrometer orbiting on

142 the national aeronautics and space administration (NASA) Aqua spacecraft launched in May 2002, which

143 can provide accurate measurements of temperature, moisture, and other atmospheric variables (Aumann

144 et al., 2003). The data used here is water vapor vertical profiles from Level 3 monthly standard gridded

145 retrieval product version 6, AIRS3STM (Susskind et al., 2014), which is available at

146 http://disc.sci.gsfc.nasa.gov. The water vapor data contains 8 levels from 1000 and 300 hPa with a

147 latitudinal and longitudinal grid of $1° \times 1°$, derived from the average of twice observations in two orbital

148 overpasses per day. The ascending and descending orbits have equatorial crossing time at 13:30 local

149 time (LT) and 1:30 LT, respectively.

154 Oceanic Niño index (ONI) is applied to discuss the correlation between the ENSO and the observed

155　water vapor anomaly. ONI is the measurement of ENSO strength, which is provided by the NOAA at

156　https://catalog.data.gov/dataset/climate-prediction-center-cpcoceanic-nino-index/. The ONI is defined as

157　a 3-month moving average of extended reconstructed sea surface temperature (ERSST) V5 sea surface

158　temperature anomalies in the Niño3.4 region at 5°N-5°S and 120°-170°W (Huang et al., 2017).

159　　Cloud occurrence probability and OLR flux are also examined since they are sensitive to water vapor

160　variation (Stevens et al., 2017; Soden et al. 2008). The OLR data is measured by the NOAA-18 satellite,

161　which travel in sun-synchronous orbit with a 13:55 LT equatorial crossing time (Kramer, 2002). We use

162　the monthly OLR data between 2005 and 2019 from the NOAA archives with a latitudinal and

163　longitudinal grid of $2.5° \times 2.5°$ (Liebmann and Smith, 1996), which can be accessed through the website

164　of https://www.esrl.noaa.gov/psd/data/gridded/data.interp_OLR.html/. Cloud-aerosols lidar and infrared

165　pathfinder satellite observations (CALIPSO) are able to clearly identify cloud vertical structure (Winker

166　et al., 2007). The satellite has a sun-synchronous orbit with an equatorial crossing time around

167　1:30/13:30 LT (Stephens et al., 2002). Here, we use the CALIPSO Version 1.00 lidar level 3 cloud

168　occurrence monthly data in a latitudinal and longitudinal grid of $2° \times 2.5°$ with an altitude resolution of

169　60 m above the mean sea level, and the available data is from June 2006 to December 2016, downloaded

170　from the website of the NASA at https://eosweb.larc.nasa.gov/project/calipso/cloud_occurrence_table/.

171

172　**3 Water Vapor Anomaly**

173　**3.1 Water Vapor Anomaly during El Niño Winter**

174　　We derive the profile of specific humidity from the radiosonde observations according to Eqs. (1-3),

175　and then calculate the monthly mean specific humidity. The monthly mean specific humidities in all the

176　same months are further averaged to obtain the monthly climatic normal, thus the monthly mean water

177   vapor anomaly is determined from the monthly mean series by subtracting the corresponding month

178   climatic normal. Figure 1 shows the monthly mean specific humidity anomaly based on the radiosonde

179   observations at Koror, Yap, Guam, Truk and Ponape from January 2005 to December 2019. Atmospheric

180   water vapor is mainly concentrated below 8 km, thus the large water vapor anomaly also occurs below 8

181   km. It can be seen from Fig. 1 that the observed water vapor anomaly is remarkably negative over the

182   five stations in the super El Niño winter of 2015-2016. The negative anomaly in the water vapor reaches

183   the peak values of -2.06 g kg^{-1} around 3 km in January at Koror, -3.2 g kg^{-1} around 3 km in February at

184   Yap, -2.39 g kg^{-1} around 2.5 km in January at Guam, -2.29 g kg^{-1} around 3.5 km in February at Truk and

185   -2.66 g kg^{-1} around 2.5 km in February at Ponape, respectively. In the 2006/07, 2009/10 and 2018/19 El

186   Niño winters, the observed water vapor also exhibits the negative anomalies in the lower and middle

187   troposphere. We derive the monthly mean specific humidity anomaly from the reanalysis data at the

188   radiosonde stations during the same period, which is also presented in Fig. 1. The ERA5 reanalysis

189   shows water vapor anomaly scenario similar to the radiosonde observation. The negative anomalies in

190   the four El Niño winters are obvious in the reanalysis data, especially the strong anomaly in the 2015/16

191   event. Hence, the El Niño events can lead to the obvious reduction of water vapor in the region.

192   With the help of the ERA5 reanalysis data, we investigate the distribution of the abnormal water vapor

193   during the four El Niño events. Here, we introduce an important scalar of column integrated water vapor

194   mass (CWV), also called precipitable water, which is expressed as (Viswanadham, 1981),

195
$$Q = \frac{1}{g}\int_{P_z}^{P_0} q\,dp \tag{4}$$

196   where Q is the CWV in units of kg m^{-2}; $g = 9.8$ m s^{-2} is the acceleration due to gravity; and the

197   pressures p_0 and p_z denote the bounds of integration, respectively. Considering that atmospheric

198   water vapor is mainly distributed below 8 km in the tropics due to the rapid decrease of water vapor with

9

199   height (Mapes et al., 2017), we choose $p_0 = 1000 \text{ hPa}$ on the ground and $p_z = 300 \text{ hPa}$ corresponding

200   to a height of about 9 km. According to Eq. (4), we calculate the CWV between 30°S and 30°N from

201   January 2005 to December 2019 based on the reanalysis data. Similarly, the monthly mean CWV and its

202   anomaly can be derived from the CWV series. Figure 2 presents the mean CWV anomalies in the four El

203   Niño winters. In the 2006/07 and 2015/16 EP El Niño events, the positive CWV anomalies appear in the

204   equatorial central and eastern Pacific, while in 2009/10 and 2018/19 CP El Niño events, the positive

205   anomalies concentrate in the central Pacific. This is consistent with previous studies (Kug et al., 2009;

206   Takahashi et al., 2013; Xu et al., 2017). The negative anomalies occur in the tropical western Pacific and

207   some tropical latitudes off the equator in both hemispheres. In the region of the five radiosonde stations,

208   the CWV anomaly is evidently negative and comparable between the 2009/10 and 2015/16 events

209   although the two events are classified into different El Niño types. Whereas in the other two events, the

210   water vapor anomaly is weak, which is in rough agreement with the radiosonde observation in Fig. 1.

211   **3.2 Relation between CWV Anomaly and ONI**

212   We choose the reanalysis CWV anomalies at the five radiosonde stations to discuss the relationship

213   between the water vapor anomaly and the ENSO. The monthly mean CWV anomaly averaged at the five

214   stations is derived from the radiosonde and reanalysis data from January 2005 to December 2019.

215   Considering that the ONI is a 3-month smoothed value, the monthly mean CWV anomaly is also

216   smoothed in a 3-month moving window. Figure 3 depicts the ONI and monthly mean CWV anomalies

217   from the radiosonde and reanalysis data. The CWV anomalies show a similar temporal evolution

218   between the observation and the reanalysis with a significant correlation coefficient R=0.83, but a

219   negative correlation to the ONI with a delay of about several months. The correlation coefficient between

220   the CWV anomaly and the ONI is calculated to be -0.63 (-0.62) with a lag of 3 (2) months. One can note

from Fig. 3 that when a strong La Niña occurs with ONI=-1.64 in November 2010, the water vapor

anomaly reaches the positive maximum in February and March 2011 from the observation and reanalysis

data, respectively. However, for the 2015/16 super El Niño event with the peak of ONI=2.6 in December

2015, an extremely negative anomaly appears in both the observation and reanalysis. The negative

anomaly attains as large as -5.39 and -5.75 kg m^{-2} in February 2016 from the radiosonde and reanalysis

data, respectively. Similarly, the 2009/10 event has a large index of ONI=1.6 in November 2009, which

leads to the strong CWV anomalies of -2.45 and -3.94 kg m^{-2} in January 2010 from the radiosonde and

reanalysis data, respectively. Hence, the ENSO or SST anomaly plays an important role in the water

vapor variation in the tropical western Pacific.

4 Contribution from Tropical Circulations

4.1 Tropical Atmospheric Circulations

Besides the SST effect, evaporated sea water is carried to higher levels by the upward flow, thus the

water vapor variability in the troposphere is closely related to the atmospheric circulation. In the tropics,

there are several well-known circulations, i.e. Hadley, Walker and monsoon circulations, and each

circulation has its own features and driving force though these circulations may be highly coupled with

each other. In this way, we attempt to estimate the contributions of each tropical circulation to the

observed water vapor anomalies in the El Niño events. According to the Helmholtz's theorem, horizontal

wind velocity can be decomposed into the rotational and divergent winds,

$$\vec{V}_H = \vec{V}_\Psi + \vec{V}_\Phi = \vec{k} \times \nabla\Psi - \nabla\Phi \tag{5}$$

where Ψ is the stream function, Φ is the velocity potential; $\vec{k}$ is the unit vector in the vertical

direction; and $\vec{V}_H$, $\vec{V}_\Psi$ and $\vec{V}_\Phi$ are the horizontal, rotational and divergent wind velocities,

243 respectively. Thermal driving force resulted from differential heating and temperature contrast is

244 essential to cause atmospheric convergence-divergence and vertical motion and then the formation of

245 atmospheric circulation. The stream function involved in the rotation field has no contribution to the

246 atmospheric vertical motion, while the velocity potential may be chosen as the indicator of the

247 atmospheric circulations since it is in connection with the atmospheric convergence-divergence

248 associated with the upward and downward motions in the tropical region (Kanamitsu and Krishnamurti,

249 1978; Newell et al., 1996; Wang, 2002). Because atmospheric water vapor comes mainly from the lower

250 atmosphere through transport of ascending flow, we selected the velocity potential at 850 hPa to

251 represent the characteristics of the tropical circulations in the lower troposphere since the pressure level

252 was extensively used to investigate the lower atmospheric circulation (Wang, 2002; Weng et al., 2008;

253 Zhao et al., 2010). The divergence and velocity potential fields are calculated by using the ECMWF

254 reanalysis horizontal winds at 850 hPa according to the following equation (Krishnamurti, 1971; Tanaka

255 et al., 2004),

$$D = \nabla \cdot \vec{V}_H = -\nabla^2 \Phi \tag{6}$$

257 where D is the divergence of horizontal wind. In Eq. (6), the negative sign means that the divergent wind

258 flows from the large velocity potential to the small velocity potential.

259 Based on the different driving mechanisms and movement features, Tanaka et al. (2004)

260 decomposed the tropical circulation in the upper troposphere (200 hPa) into the Hadley, Walker and

261 monsoon circulations, which have an advantage to quantitatively evaluate the intensity of the three

262 tropical circulations by means of the separation of the velocity potential into three orthogonal spatial

263 patterns. Subsequently, Takemoto and Tanaka (2007) used these circulation definitions to analyze the

264 Hadley, Walker, and monsoon circulations at 850 hPa of the lower troposphere, and compared the three

265   circulation components with those in the upper troposphere (200 hPa), which indicated that the velocity

266   potential intensities could be an index of each circulation in the lower troposphere without a notable

267   influence from the surface. Considering that atmospheric water vapor is mainly distributed below 8 km,

268   directly relevant to the lower tropospheric circulation, we follow the definitions and methodology

269   proposed by Tanaka et al. (2004) to obtain these tropical circulations at 850 hPa level for investigating

270   their contributions to the observed water vapor anomaly in the four El Niño events. The velocity potential

271   is divided as (Tanaka et al., 2004),

$$\Phi(x,y,t) = [\Phi(t,y)] + \overline{\Phi^*}(x,y) + \Phi^{*\prime}(x,y,t) \tag{7}$$

273   where x, y and t are the longitude, latitude and time, respectively. The square brackets and asterisk denote

274   the zonal mean and the deviation from the zonal mean, respectively, and the overbar and prime denote the

275   annual mean and the departure from the annual mean, respectively. The first term on the right of Eq. (7) is

276   the zonal mean component of the velocity potential field, defined as the Hadley circulation because this

277   circulation, driven by the large-scale meridional differential heating, may be treated as axisymmetric. The

278   second and third terms on the right are the annual mean of the deviation from the zonal mean and the

279   deviation from the annual mean, respectively. The third term is regarded to be the monsoon circulation

280   since the monsoon circulation has the conspicuous seasonal variability as the sea-land heat contrast

281   changes. The second term is referred to as the Walker circulation. The separation is not perfect for the

282   Walker circulation without seasonal variation, as pointed out by Tanaka et al. (2004). The Walker

283   circulation is induced by the different SST along the equator. Considering that the El Niño usually lasts for

284   more than a year with the maximum ONI in winter, we chose the period of June to the next May to

285   estimate the Walker circulation, and then obtain the Walker circulation anomaly during El Niño relative to

286   its climatic average. In this way, the problem may not be very serious. The definitions and decomposition

13

287   of the tropical circulations have extensively been used to study the influences of SST warming pattern on

288   the interannual variation and long-term trend of the Hadley, Walker and monsoon circulations in

289   association with hydrological cycle (Tanaka et al., 2005; Park and Sohn, 2008; Li and Feng, 2013; Ma and

290   Xie, 2013).

291   We firstly calculate the divergence field of the horizontal wind at 850 hPa from 2005 to 2019 by

292   using the reanalysis horizontal wind data, and then the velocity potential is deduced according to Eq. (6),

293   which is equivalent to solving Poisson equation. Next, according to Eq. (7), the velocity potential filed is

294   decomposed into the Hadley, Walker and monsoon circulation components. In this way, their monthly

295   climatic mean is derived from their time series, respectively. Figure 4 presents the climatic means of the

296   velocity potential and divergent wind fields in DJF. We choose the velocity potential as the proxy of the

297   circulation intensity, thus the intensity of the tropical circulation in winter can clearly be seen from Fig. 4.

298   The prominent negative peak of about -81×10^5 m^2 s^{-1} in the velocity potential is situated in the western

299   Pacific warm pool, thus there is the convergence center of horizontal wind field, which induces the rising

300   motion in the lower troposphere over the region, including the five radiosonde stations. Hence, the

301   atmospheric water vapor is abundant in this region due to the transport by the strong ascending flow. On

302   the contrary, the maximum velocity potential of 48×10^5 m^2 s^{-1} appears in the northeast Pacific Ocean and

303   the southern part of the North American continent, meaning a downward motion associated with the

304   divergence center over there, as well as less water vapor relative to the western Pacific warm pool region.

305   **4.2 Atmospheric Circulation Anomalies**

306   Next, we focus on the tropical circulation anomaly in the four El Niño events. Figure 5 illustrates the

307   velocity potential and divergent wind anomalies at 850 hPa in the four winters. Here, we define the

308   velocity potential value as the circulation index with the units measured by 10^5 m^2 s^{-1}, and accordingly,

14

the velocity potential anomaly is regarded as the index of the circulation anomaly. As a consequence, the

positive index of the circulation anomaly indicates the weakened convergence and rising motion or the

strengthened divergence and sinking motion, and vice versa for the negative index of the circulation

anomaly. Hence, the positive and negative indices mean the decrease and increase of water vapor in the

troposphere due to the vertical transport change, respectively. In Fig. 5, the positive index of the

circulation anomaly occurs in the western Pacific, especially in the 2009/10 and 2015/16 El Niño winters,

thus the ascending motion is suppressed over there, and the negative water vapor anomalies are recorded

in the radiosonde observation. On the contrary, there is the negative index in the equatorial eastern

Pacific, which causes that the descending flow is suppressed. Correspondingly, the positive CWV

anomaly over the equatorial eastern Pacific can be seen from Fig. 2.

According to Eq. (7), we calculate the velocity potential of the Hadley, Walker and monsoon

circulations and their anomaly indices at 850 hPa from the reanalysis data. Figure 6 presents the velocity

potential and anomaly index of the Hadley circulation in the four El Niño winters. Now that the Hadley

circulation is a tropical circulation driven by the meridional differential heating in the global radiative

process (Oort and Yienger, 1996), this large-scale circulation is very similar in different winters with the

circulation index increasing from the negative peak at about 12°S to positive peak at 23°N, and is little

affected by El Niño with the anomaly index less than 2×10^5 m^2 s^{-1}, or 2 units. Even so, the pattern of the

Hadley circulation anomaly is distinguished between the EP El Niño and CP El Niño. During the 2018/19

(2009/10) CP El Niño winters, the index of the Hadley circulation anomaly is positive over the entire

tropics with the maximum of 1.74 (1.65) units at 3°N (2°N). Whereas, in the 2006/07 and 2015/16 EP El

Niño winters, the positive index is located at about 5°N-30°N, and the negative index occurs over about

30°S-5°N. Li and Feng (2012) suggested that the different patterns of the Hadley circulation anomalies

between the CP and EP El Niños are associated with the contrasting underlying thermal structure changes because the maximum of the zonal-mean SST anomalies is moved northward to about 10°N in the CP event relative to the maximum around the equator in the EP event. At the five radiosonde sites, the averaged anomaly index is 0.29, 1.56, 0.65 and 1.37 units in the 2006/07, 2009/10, 2015/06 and 2018/19 winters, respectively, indicating that the Hadley circulation is too stable to have a significant impact on the water vapor variation.

Figure 7 depicts the velocity potential and anomaly index of the Walker circulation at 850 hPa in the El Niño winters. Relative to the Hadley circulation, the Walker circulation is the local circulation formed over the tropical Pacific with intense ascending flow in the western Pacific and descending flow in the eastern Pacific, thus the circulation has a high variability with the SST anomaly caused by ocean current. As the Walker circulation is directly related to ENSO, the scenario of the Walker circulation anomalies is roughly consistent with each other among the four El Niño events. In general, the positive and negative indices of the Walker circulation anomaly are located in the western and eastern Pacific, opposite to the circulation index, respectively, which illustrates that the Walker circulation anomaly in El Niño suppresses the strong rising in the western Pacific and sinking in the eastern Pacific. Nevertheless, the strength of the circulation anomaly is the significant difference among the four events. In the 2015/16 winter, the Walker circulation anomaly, with the peak indices as large as 26.8 and -27.7 units in the equatorial Pacific, are much stronger than in the other three winters. Hence, the Walker circulation variation plays a key role in the CWV anomaly during the 2015/16 super El Niño event.

The velocity potential and anomaly index of the monsoon circulation in the four El Niño winters are plotted in Fig. 8. The monsoon circulation in the lower atmosphere blows from the land to the sea in winter, thus it can be seen from Fig. 8 that the pattern of the monsoon circulation is evidently different

from that of the Walker circulation shown in Fig. 7. The anomaly of the monsoon circulation is sensitive

to the type of El Niño, which is also distinguished from that of the Walker circulation. Early studies

showed that the CP and EP El Niños have different effects on the Indian and eastern Asian monsoon

rainfall (Weng et al., 2008; Wang et al., 2013). The monsoon circulation anomaly in the radiosonde

stations has the index around zero in the EP El Niño events, which is far weaker relative to the large

positive index in the CP El Niño events, similar to previous investigation (Fan et al, 2017). In the

2009/10 El Niño event, the pronounced anomaly with the peak index of 17.8 units takes place in the

western Pacific, which implies that the monsoon circulation anomaly has an important influenced on the

negative water vapor anomaly in the radiosonde observation.

4.3 Contribution to Water Vapor Anomaly

We estimate the contributions of the Hadley, Walker and monsoon circulation anomalies to the

water vapor anomaly observed by the radiosonde in the four El Niño events by means of comparing the

indices of the circulation anomalies. Figure 9 illustrates the indices of the circulation anomalies at 850

hPa and the CWV anomalies derived from the radiosonde and reanalysis data, and these circulation

anomaly indices and CWV anomalies are the values averaged at the five radiosonde sites in winter. It can

be seen from Figure 9 that qualitatively, the CWV anomalies in the reanalysis and radiosonde data

increase with the increasing index of the total circulation anomaly. As discussed above, the contribution

of the Hadley circulation anomaly is very small with the maximum of only 1.56 units in the 2009/10

event. The anomaly of the Walker circulation makes a considerable contribution in each case, especially

for the EP El Niño events, it is the strongest in the three tropical circulation anomalies. The index of the

Walker circulation anomaly counts for 92.3% of the total anomaly index (23.89 units) in the 2015/16 El

Niño winter, and even exceeds the total index in the 2006/07 event owing to the negative anomaly of the

17

375 monsoon circulation. The anomaly of the monsoon circulation shows an evident change from one event

376 to another because it is sensitive to the local heat contrast and the El Niño shift. In the western Pacific,

377 the CP El Niño can lead to the obvious positive anomaly of the monsoon circulation. The index of the

378 monsoon circulation anomaly is about 69.7% (44.7%) of the total anomaly index in the 2009/10 (2018/19)

379 CP El Niño winter. Consequently, for the two intense El Niño events, the water vapor anomaly is caused

380 mainly by the Walker circulation anomaly in the 2015/16 EP event but by the monsoon circulation

381 anomaly in the 2009/10 CP event, respectively. The Walker and monsoon circulation anomalies nearly

382 equally (oppositely) contribute to the CWV anomaly in the 2018/19 (2006/07) event. Therefore, except

383 the Hadley circulation anomaly, the Walker and monsoon circulation anomalies may have the

384 considerable differences in the contributions to the water vapor variation in different El Niño events. In

385 addition, in the 2015/16 and 2018/19 winters, the reanalysis CWV anomalies of -4.34 and -1.30 kg m^{-2}

386 are roughly consistent with -4.46 and -1.54 kg m^{-2} in the radiosonde observation, respectively. However,

387 in the first two events, there is a distinct difference of the CWV anomaly between the reanalysis and

388 radiosonde data, and we will discuss the discrepancy in detail below.

389   In order to obtain the general features of water vapor and circulation anomalies in the EP and CP El

390 Niño events, we extend the reanalysis data back to 1979 to examine two types of composite El Niño

391 events. There are six EP El Niño events in the winters of 1982/83, 1986/87, 1991/92, 1997/98, 2006/07

392 and 2015/16, and five CP El Niño events in the 1994/95, 2002/03, 2004/05, 2009/10 and 2018/19 winters

393 for 41 years from 1979 to 2019, which are averaged as the composite EP and CP El Niños, respectively.

394 We calculate the CWV anomalies in the two composite events based the climatic mean CWV in 41

395 winters, and the corresponding velocity potential and divergent wind anomalies of the Walker, monsoon

396 and total circulations from the reanalysis horizontal wind at 850 hPa, which are shown in Fig. 10. The

397   Hadley circulation anomaly (not presented) is very small, and its patterns in the composite EP and CP El

398   Niños are also analogous to those in the EP and CP events shown in Fig. 6, respectively. On the whole,

399   Fig. 10 illustrates that the total circulation anomaly is stronger in EP event than in CP event, and then the

400   CWV anomaly is larger in EP event relative to that in CP event. The Walker circulation plays an

401   important role in the total circulation anomaly, especially in EP El Niño. Despite significant variability

402   from one event to another, the monsoon circulation anomaly has not only a larger proportion of the total

403   anomaly but also slightly higher intensity in CP El Niño than in EP El Niño. At the five radiosonde

404   stations, the composite events indicate that the CWV anomaly is about -4.36 and -1.74 kg m^{-2} in EP and

405   CP El Niños, respectively. The index of the Walker circulation anomaly accounts for about 75.8% (47.8%)

406   of the total anomaly index in EP (CP) El Niño, while for the monsoon circulation, the anomaly index of

407   6.16 (4.66) units contributes to 49.6% (18.4%) of the total anomaly index in CP (EP) El Niño. Therefore,

408   the relative importance of the Hadley, Walker and monsoon circulation anomalies in the composite El

409   Niños is roughly in accord with that in the case study above. In addition, at the radiosonde sites, the CP

410   El Niño can generally cause an intense monsoon circulation anomaly, which is comparable to and even

411   larger than the Walker circulation anomaly, thus the CP El Niño in the winter of 2009/10 may induce a

412   quite strong monsoon circulation anomaly now that the 2009/10 event is the strongest CP El Niño from

413   the 1980s, as observed by satellite (Lee and Mcphaden, 2010).

414

415   **5 Changes in Cloud and OLR**

416   Using the cloud occurrence from the CALIPSO during June 2006 to December 2016, we calculate

417   tropical cloud fraction between 0°N and 15°N in the 2006/07, 2009/10 and 2015/16 winters and its

418   climatic mean in winter, which is shown in Fig. 11. We also compute the OLR anomalies over 30°S-30°N

419   in the four El Niño winters based on the monthly OLR data between 2005 and 2019. Figure 12 shows the

420   OLR anomalies in the four El Niño events. In the western Pacific, the strong rising flow carries abundant

421   water vapor to high level due to the convergence of horizontal wind field in winter, as shown in Fig. 4,

422   and then the water vapor condenses to form clouds as it cools, thus there is clouds over the tropical

423   western Pacific. In the El Niño events, the cloud amount decreases from about 80°E to 160°E but tends to

424   increase between about 160°E to 120°W because of the tropical circulation changes. Owing to the

425   reflection effect of cloud on OLR, the OLR change is opposite to the variation of cloud amount. In the

426   2009/10 and 2015/16 strong El Niño winters, the OLR is obviously enhanced in the tropical northwest

427   Pacific and significantly reduced in the equatorial mid-eastern Pacific as the cloud occurrence changes.

428   Hence, the cloud and OLR have a clear response to the water vapor anomaly in the El Niño events.

429   As described above, the reanalysis CWV anomaly at the radiosonde stations in the 2009/10 winter

430   has an almost same intensity as that in the 2015/16 winter, but the radiosonde observation indicates that

431   the water vapor reduction is evidently less in the 2009/10 winter than in the 2015/16 winter. As shown in

432   Figs. 11 and 12, the satellite observation shows that there exist less cloud occurrence and more OLR at

433   the radiosonde stations in the 2015/16 winter compared with in the 2009/10 winter. Therefore, this

434   supports the radiosonde observation that the water vapor over the radiosonde stations in the 2009/10

435   winter may be moister than in the reanalysis.

436

437   **6 Discussion**

438   In the ERA5 reanalysis data, water vapor is calculated by a humidity analysis scheme introduced by

439   Hólm (2003), which involves nonlinear transformation of the humidity control variable to render the

440   humidity background errors nearly Gaussian. The transformation normalizes relative humidity

441   increments by a factor that varies as a function of background errors of relative humidity and vertical

level (Dee et al., 2011). For the ERA5 humidity analysis, measurements from radiosonde, surface synoptic observation, aircraft, and satellite observations are assimilated (Andersson et al., 2007). To date, the reliability and accuracy of ERA5 water vapor products have extensively been estimated. Overall, ERA5 retrieved precipitable water vapor (PWV) performs well over the Indian Ocean (Lees et al, 2020), central Asia (Jiang et al, 2019), Antarctic (Ye et al, 2007), East African tropical region (Ssenyunzi et al, 2020) and Varanasi (Kumar et al, 2020) via comparisons with ground-based observations, satellite retrievals and other reanalysis datasets. Nevertheless, some discrepancies can be noticed over small tropical islands characterized by steep orography (Lees et al, 2020), and it is reported that although PWV from the ERA5 reanalysis is in good agreement with the retrieval from Global Navigation Satellite System over 268 stations, a bias of 4 mm PWV in the southwest of South America and western China due to the limit of terrains and fewer observations (Wang et al, 2020).

Since the CWV anomalies look more or less different between the radiosonde and reanalysis data, we compare the CWV in the ERA5 reanalysis with that in the radiosonde and satellite observations at the five stations, and attempt to explain the different CWV anomalies between the reanalysis data and radiosonde observation in the 2006/07 and 2009/10 events. By using the reanalysis data and measurements of radiosonde and AIRS on Aqua satellite for the 15 year period from 2005 to 2019, we calculate the monthly mean CWV at the five radiosonde sites, and Fig. 13 depicts the monthly mean CWV in winter as scatterplots of the reanalysis vs. radiosonde data and the reanalysis vs. AIRS data. And then the climatic mean difference is derived from these monthly mean CWV series in 2005-2019, which is also presented in Fig. 13. At the five stations, the monthly mean CWV in winter is distributed between 30 and 60 kg m^{-2} in all the three datasets, and the CWV is obviously shifted to the low values in the El Niño winter, indicating the negative anomaly in the El Niño event. The correlation of the mean CWV

464 series between the reanalysis and observations is quite high with the minimum coefficient of 0.88, and all

465 the root mean square (RMS) of the mean CWV differences between the reanalysis and observations is

466 less than 2.32 kg m^{-2}. Meanwhile, the difference of the climatic mean CWV is mainly concentrated in the

467 range of 0-2 kg m^{-2} except several months at the Guam station, thus the relative difference of the monthly

468 mean CWV between the reanalysis and observations is generally smaller than 5%. These comparison and

469 analysis confirm a fine confidence level of the ERA5 reanalysis and observational datasets. Nevertheless,

470 there are still very small discrepancies among these data, and the discrepancy is relatively larger between

471 the radiosonde and reanalysis data than between the satellite and reanalysis data, which may be attributed

472 to a possible cause of different sampling times between the radiosonde and AIRS. It can be noted from

473 Fig. 13 that the red dots representing the reanalysis vs. radiosonde data in the 2009/10 winter show a

474 relatively scatter around the symmetric axis, indicating a relatively large discrepancy of the CWV

475 anomalies between the reanalysis data and radiosonde observation in this event, as previous reports of

476 some discrepancies over small tropical islands or in the region with fewer observations (Lees et al, 2020;

477 Wang et al, 2020). As comparison to the reanalysis data, the CWV derived from AIRS also shows the

478 largest difference of 1.31 kg m^{-2} in the 2009/10 event, while the differences are less than 1 kg m^{-2} in the

479 other three events.

480 Based on specific humidity in the reanalysis and radiosonde data, the CWV is calculated to be 44.87

481 (44.10), 43.06 (40.23), 41.16 (39.83) and 44.07 (42.87) kg m^{-2} in the radiosonde (reanalysis) data in the

482 2006/07, 2009/10, 2015/16 and 2018/19 events, respectively. In fact, the relative difference of the CWV

483 between the radiosonde and reanalysis data is very small with only 1.7% in the 2006/07 winter, and 6.6%

484 in the 2009/10 winter. The CWV average in winter is 45.61 (44.17) kg m^{-2} in the radiosonde (reanalysis)

485 data from 2005 to 2019, thus the CWV anomaly in the radiosonde (reanalysis) data is -0.74 (-0.07) kg

486 m^{-2} in the 2006/07 event, and -2.55 (-3.94) kg m^{-2} in the 2009/10 event. This causes that the discrepancy

487 of the CWV anomaly looks considerably large in Fig. 9, especially in the 2006/07 event, but the

488 differences of both the CWV and CWV anomaly values are small between the radiosonde and reanalysis.

489 Even so, the relatively large discrepancy between the reanalysis data and the radiosonde and AIRS

490 observations in the 2009/10 event, as shown in Figs. 1 and 13, and the cloud and OLR measurements in

491 Figs. 11 and 12 seem to suggest that the reanalysis data underestimates the tropospheric water vapor over

492 the radiosonde stations in the 2009/10 winter.

493

494 **7 Summary**

495 In the paper, we report the significantly negative water vapor anomaly in the troposphere during the

496 four El Niño winters at the five radiosonde stations in the tropical western Pacific based on the

497 radiosonde and reanalysis data for 15 years from 2005 to 2019, and study the relationship between the

498 water vapor anomaly and the El Niño index and the contribution of the different tropical circulation

499 anomalies to the observed water vapor anomaly in the El Niño events.

500 The radiosonde observation shows that the negative water vapor anomaly arises in the El Niño

501 winters, in particular, an extremely negative anomaly in the 2015/16 super El Niño event. The prominent

502 specific humidity anomaly is concentrated below 8 km of the troposphere with the peak at the height of

503 about 2.5-3.5 km. The local CWV anomaly has a large negative correlation coefficient of -0.63 with the

504 ONI in the Niño3.4 region, but with a lag of about 2-3 months. The reanalysis data reveals that the

505 negative water vapor anomaly widely occurs in the tropical northwest Pacific, while correspondingly, the

506 positive anomaly takes place in the equatorial mid-eastern Pacific. The 2015/16 El Niño event, with

507 ONI=2.6, is the strongest during the 15 years, leading to the extreme anomaly in the water vapor over the

508   tropical Pacific.

509   The atmospheric water vapor from tropical sea water evaporation is affected not only by the SST, but

510   also by the vertical motion of the atmosphere which can transport the water vapor from the near-sea

511   surface to the high level. By using the definitions and method introduced by Tanaka et al. (2004), we

512   decompose the tropical circulation into the Hadley, Walker and monsoon circulations to estimate their

513   contributions to the observed water vapor anomaly in the four El Niño events. In general, the tropical

514   circulation anomaly in the El Niño winter is characterized by divergence (convergence) at 850 hPa in the

515   tropical western (eastern) Pacific, thus the CWV decreases over the tropical western Pacific as the

516   ascending flow is suppressed. As the large-scale meridional circulation driven by the differential heating,

517   the variation of the Hadley circulation is pretty small with the anomaly index less than 2 units. At the

518   radiosonde stations, the anomaly of the Walker circulation makes a considerable contribution to the total

519   anomaly in all the El Niño winters, especially in the 2006/07 and 2015/16 EP El Niño event. The

520   monsoon circulation exhibits an obvious variability from one event to another, and its anomaly is large in

521   the 2009/10 and 2018/19 CP El Niño winters and small in the 2006/07 and 2015/16 EP El Niño winters.

522   Therefore, the observed water vapor anomaly is caused mainly by the Walker circulation anomaly in the

523   2015/16 super EP event but by the monsoon circulation anomaly in the 2009/10 strong CP event,

524   respectively. Based on the reanalysis data back to 1979, we examine the general features of water vapor

525   and circulation anomalies in the two types of composite El Niño events. The roles of the Hadley, Walker

526   and monsoon circulations in the composite EP and CP El Niños are consistent with those in the EP and

527   CP case events.

528   Because of the reduction in the upward transport of water vapor over the tropical western Pacific in

529   the El Niño events, the satellite observation shows that relative to the climatic means, the cloud decreases,

24

530   and the OLR is accordingly strengthened, in particular, during the strong El Niño winters of 2009/10 and

531   2015/16. In addition, a detailed comparison of water vapor in the reanalysis, radiosonde and satellite data

532   shows a high confidence level of these datasets, nevertheless, the reanalysis seems to slightly

533   underestimate the water vapor over the five radiosonde stations in the 2009/10 winter.

534

535

543

546

548

551

References

Andersson, E., Hólm, E., Bauer, P., Beljaars, A., Kelly, G. A., McNally, A. P., Simmons, A. J., Thépaut, J. N., and Tompkins, A. M.: Analysis and forecast impact of the main humidity observing systems, Q. J. R. Meteorol. Soc., https://doi.org/10.1002/qj.112, 2007.

Ashok, K., Behera, S. K., Rao, S. A., Weng, H., and Yamagata, T.: El Niño Modoki and its possible teleconnection, J. Geophys. Res., 112, https://doi.org/10.1029/2006jc003798, 2007.

Aumann, H. H., Chahine, M. T., Gautier, C., Goldberg, M. D., Kalnay, E., McMillin, L. M., Revercomb, H., Rosenkranz, P. W., Smith, W. L., Staelin, D. H., Strow, L. L., and Susskind, J.: AIRS/AMSU/HSB on the aqua mission: design, science objectives, data products, and processing systems, IEEE Trans. Geosci. Remote Sens., 41, 253-264, https://doi.org/10.1109/tgrs.2002.808356, 2003.

Avery, M. A., Davis, S. M., Rosenlof, K. H., Ye, H., and Dessler, A. E.: Large anomalies in lower stratospheric water vapour and ice during the 2015–2016 El Niño, Nat. Geosci., 10, 405-409, https://doi.org/10.1038/ngeo2961, 2017.

Dai, A. and Wigley, T. M. L.: Global patterns of ENSO-induced precipitation, Geophys. Res. Lett., 27, 1283-1286, https://doi.org/10.1029/1999gl011140, 2000.

Dee, D. P., Uppala, S. M., Simmons, A. J., Berrisford, P., Poli, P., Kobayashi, S., Andrae, U., Balmaseda, M. A., Balsamo, G., Bauer, P., Bechtold, P., Beljaars, A. C. M., van de Berg, L., Bidlot, J., Bormann, N., Delsol, C., Dragani, R., Fuentes, M., Geer, A. J., Haimberger, L., Healy, S. B., Hersbach, H., Hólm, E. V., Isaksen, L., Kållberg, P., Köhler, M., Matricardi, M., McNally, A. P., Monge-Sanz, B. M., Morcrette, J. J., Park, B. K., Peubey, C., de Rosnay, P., Tavolato, C., Thépaut, J. N., and Vitart, F.: The ERA-Interim reanalysis: configuration and performance of the data assimilation system, Q. J. R. Meteorol. Soc., 137, 553-597, https://doi.org/10.1002/qj.828, 2011.

574 Dunkerton, T. J.: The quasi-biennial oscillation of 2015-2016: Hiccup or death spiral?, Geophys. Res. Lett.,

575   43, 10,547-510,552, https://doi.org/10.1002/2016gl070921, 2016.

576 Fan, F., Dong, X., Fang, X., Xue, F., Zheng, F., and Zhu, J.: Revisiting the relationship between the South

577   Asian summer monsoon drought and El Niño warming pattern, Atmos. Sci. Let., 18, 175-182,

578   https://doi.org/10.1002/asl.740, 2017.

579 Gasparin, F. and Roemmich, D.: The strong freshwater anomaly during the onset of the 2015/2016 El

580   Niño, Geophys. Res. Lett., 43, 6452-6460, https://doi.org/10.1002/2016gl069542, 2016.

581 Gu, G. and Adler, R. F.: Precipitation, temperature, and moisture transport variations associated with two

582   distinct ENSO flavors during 1979–2014, Climate Dyn., 52, 7249-7265,

583   https://doi.org/10.1007/s00382-016-3462-3, 2016.

584 Held, I. M. and Soden, B. J.: Water vapor feedback and global warming, Annu. Rev. Energy Env., 25,

585   441-475, https://doi.org/10.1146/annurev.energy.25.1.441, 2000.

586 Hersbach, H., Bell, B., Berrisford, P., Hirahara, S., Horányi, A., Muñoz-Sabater, J., Nicolas, J., Peubey, C.,

587   Radu, R., Schepers, D., Simmons, A., Soci, C., Abdalla, S., Abellan, X., Balsamo, G., Bechtold, P.,

588   Biavati, G., Bidlot, J., Bonavita, M., Chiara, G., Dahlgren, P., Dee, D., Diamantakis, M., Dragani, R.,

589   Flemming, J., Forbes, R., Fuentes, M., Geer, A., Haimberger, L., Healy, S., Hogan, R. J., Hólm, E.,

590   Janisková, M., Keeley, S., Laloyaux, P., Lopez, P., Lupu, C., Radnoti, G., Rosnay, P., Rozum, I.,

591   Vamborg, F., Villaume, S., and Thépaut, J. N.: The ERA5 global reanalysis, Q. J. R. Meteorol. Soc.,

592   146, 1999-2049, https://doi.org/10.1002/qj.3803, 2020.

593 Hill, K. J., Taschetto, A. S., and England, M. H.: South American rainfall impacts associated with inter-El

594   Niño variations, Geophys. Res. Lett., 36, https://doi.org/10.1029/2009gl040164, 2009.

595 Huang, B. Y., Thorne, P. W., Banzon, V. F., Boyer, T., Chepurin, G., Lawrimore, J. H., Menne, M. J., Smith,

T. M., Vose, R. S., and Zhang, H. M.: Extended reconstructed sea surface temperature, version 5 (ERSSTv5): Upgrades, validations, and intercomparisons, J. Climate, 30, 8179-8205, https://doi.org/10.1175/jcli-d-16-0836.1, 2017.

Hólm, E. V.: Revision of the ECMWF humidity analysis: Construction of a Gaussian control variable. Proc. Workshop on Humidity Analysis, Reading, United Kingdom, ECMWF/GEWEX, 1–6, 2003.

Ishida, A., Kashino, Y., Hosoda, S., and Ando, K.: North-south asymmetry of warm water volume transport related with El Niño variability, Geophys. Res. Lett., 35, https://doi.org/10.1029/2008gl034858, 2008.

Jiang, J., Zhou, T., and Zhang, W.: Evaluation of satellite and reanalysis precipitable water vapor data sets against radiosonde observations in Central Asia, Earth Space Sci., 6, 1129-1148, https://doi.org/10.1029/2019ea000654, 2019.

Kanamitsu, M. and Krishnamurti, T. N.: Northern summer tropical circulations during drought and normal rainfall months, Mon. Weather Rev., 106, 331-347, https://doi.org/10.1175/1520-0493(1978)106<0331:Nstcdd>2.0.Co;2, 1978.

Krishnamurti, T. N.: Tropical east-west circulations during the northern summer, J. Atmos. Sci., 28, 1342-1347, https://doi.org/10.1175/1520-0469(1971)028<1342:TEWCDT>2.0.CO;2, 1971.

Kug, J.-S., Jin, F.-F., and An, S.-I.: Two types of El Niño events: cold tongue El Niño and warm pool El Niño, J. Climate, 22, 1499-1515, https://doi.org/10.1175/2008JCLI2624.1, 2009.

Kumar, A., Kumar, S., Pratap, V., and Singh, A. K.: Performance of water vapour retrieval from MODIS and ECMWF and their validation with ground based GPS measurements over Varanasi, J. Earth Syst. Sci., 130, https://doi.org/10.1007/s12040-020-01529-3, 2021.

Kramer, H. J.: Observation of the earth and its environment: Survey of missions and sensors. Springer

Science & Business Media. p. 737. ISBN 978-3-540-42388-1, 2002.

L'Heureux, M. L., Takahashi, K., Watkins, A. B., Barnston, A. G., Becker, E. J., Di Liberto, T. E., Gamble, F., Gottschalck, J., Halpert, M. S., Huang, B., Mosquera-Vásquez, K., and Wittenberg, A. T.: Observing and predicting the 2015/16 El Niño, Bull. Amer. Meteor. Soc., 98, 1363-1382, https://doi.org/10.1175/bams-d-16-0009.1, 2017.

Lanzante, J. R.: Resistant, robust and non-parametric techniques for the analysis of climate data: Theory and examples, including applications to historical radiosonde station data, Int. J. Climatol., 16, 1197-1226, https://doi.org/10.1002/(SICI)1097-0088(199611)16:11<1197::AID-JOC89>3.0.CO;2-L, 1996.

Lees, E., Bousquet, O., Roy, D., and Bellevue, J. L. d.: Analysis of diurnal to seasonal variability of Integrated Water Vapour in the South Indian Ocean basin using ground-based GNSS and fifth-generation ECMWF reanalysis (ERA5) data, Q. J. R. Meteorol. Soc., 147, 229-248, https://doi.org/10.1002/qj.3915, 2020.

Lee, S.-K., Mapes, B. E., Wang, C., Enfield, D. B., and Weaver, S. J.: Springtime ENSO phase evolution and its relation to rainfall in the continental U.S, Geophys. Res. Lett., 41, 1673-1680, https://doi.org/10.1002/2013gl059137, 2014.

Lee, T. and McPhaden, M. J.: Increasing intensity of El Niño in the central-equatorial Pacific, Geophys. Res. Lett., 37, https://doi.org/https://doi.org/10.1029/2010GL044007, 2010.

Li, J. and Feng, J.: Contrasting impacts of two types of ENSO on the boreal spring Hadley circulation, J. Climate, 26, 4773-4789, https://doi.org/10.1175/jcli-d-12-00298.1, 2013.

Li, Z., Li, Y., Bonsal, B., Manson, A. H., and Scaff, L.: Combined impacts of ENSO and MJO on the 2015 growing season drought on the Canadian Prairies, Hydrol. Earth Syst. Sci., 22, 5057-5067,

https://doi.org/10.5194/hess-22-5057-2018, 2018.

Liebmann, B. and Smith, C. A.: Description of a complete (interpolated) outgoing longwave radiation dataset, Bull. Amer. Meteor. Soc., 77, 1275-1277, 1996.

López-Parages, J. and Rodríguez-Fonseca, B.: Multidecadal modulation of El Niño influence on the Euro-Mediterranean rainfall, Geophys. Res. Lett., 39, https://doi.org/https://doi.org/10.1029/2011GL050049, 2012.

Ma, J. and Xie, S.-P.: Regional patterns of sea surface temperature change: A source of uncertainty in future projections of precipitation and atmospheric circulation, J. Climate, 26, 2482-2501, https://doi.org/10.1175/jcli-d-12-00283.1, 2013.

Madenach, N., Carbajal Henken, C., Preusker, R., Sourdeval, O., and Fischer, J.: Analysis and quantification of ENSO-linked changes in the tropical Atlantic cloud vertical distribution using 14 years of MODIS observations, Atmos. Chem. Phys., 19, 13535-13546, https://doi.org/10.5194/acp-19-13535-2019, 2019.

Mapes, B., Chandra, A. S., Kuang, Z., and Zuidema, P.: Importance profiles for water vapor, Surv. Geophys., 38, 1355-1369, https://doi.org/10.1007/s10712-017-9427-1, 2017.

Mariotti, A.: How ENSO impacts precipitation in southwest central Asia, Geophys. Res. Lett., 34, https://doi.org/10.1029/2007gl030078, 2007.

Massie, S., Lowe, P., Tie, X., Hervig, M., Thomas, G., and Russell, J.: Effect of the 1997 El Niño on the distribution of upper tropospheric cirrus, J. Geophys. Res.-Atmos., 105, 22725-22741, https://doi.org/10.1029/2000jd900322, 2000.

Murray, F. W.: On the computation of saturation vapor pressure, J. Appl, Meteorol., 6, 203-204, https://doi.org/10.1175/1520-0450(1967)006<0203:OTCOSV>2.0.CO;2 1967.

662 Newell, R. E., Zhu, Y., Browell, E. V., Read, W. G., and Waters, J. W.: Walker circulation and tropical

663 upper tropospheric water vapor, J. Geophys. Res.-Atmos., 101, 1961-1974,

664 https://doi.org/10.1029/95jd02275, 1996.

665 Newman, P. A., Coy, L., Pawson, S., and Lait, L. R.: The anomalous change in the QBO in 2015-2016,

666 Geophys. Res. Lett., 43, 8791-8797, https://doi.org/10.1002/2016gl070373, 2016.

667 Okazaki, A., Satoh, Y., Tremoy, G., Vimeux, F., Scheepmaker, R., and Yoshimura, K.: Interannual

668 variability of isotopic composition in water vapor over western Africa and its relationship to ENSO,

669 Atmos. Chem. Phys., 15, 3193-3204, https://doi.org/10.5194/acp-15-3193-2015, 2015.

670 Oort, A. H. and Yienger, J. J.: Observed interannual variability in the Hadley circulation and its connection

671 to ENSO, J. Climate, 9, 2751-2767,

672 https://doi.org/10.1175/1520-0442(1996)009<2751:OIVITH>2.0.CO;2, 1996.

673 Paek, H., Yu, J.-Y., and Qian, C.: Why were the 2015/2016 and 1997/1998 extreme El Niños different?,

674 Geophys. Res. Lett., https://doi.org/10.1002/2016gl071515, 2017.

675 Palmeiro, F. M., Iza, M., Barriopedro, D., Calvo, N., and García-Herrera, R.: The complex behavior of El

676 Niño winter 2015-2016, Geophys. Res. Lett., 44, 2902-2910, https://doi.org/10.1002/2017gl072920,

677 2017.

678 Park, S.-C. and Sohn, B.-J.: Recent trend of Hadley and Walker circulation shown in water vapor transport

679 potential, in: 20th Conference on climate variability and change, General climate studies: poster

680 session, New York, United States, 21 January 2008, P2.18, 2008.

681 Permana, D. S., Thompson, L. G., and Setyadi, G.: Tropical West Pacific moisture dynamics and climate

682 controls on rainfall isotopic ratios in southern Papua, Indonesia, J. Geophys. Res.-Atmos., 121,

683 2222-2245, https://doi.org/10.1002/2015jd023893, 2016.

684 Quartly, G. D., Srokosz, M. A., and Guymer, T. H.: Changes in oceanic precipitation during the 1997-98

685   El Niño, Geophys. Res. Lett., 27, 2293-2296, https://doi.org/10.1029/1999gl011311, 2000.

686 Sandeep, S. and Ajayamohan, R. S.: Modulation of winter precipitation dynamics over the Arabian Gulf

687   by ENSO, J. Geophys. Res.-Atmos., 123, 198-210, https://doi.org/10.1002/2017jd027263, 2018.

688 Soden, B. J., Held, I. M., Colman, R., Shell, K. M., Kiehl, J. T., and Shields, C. A.: Quantifying climate

689   feedbacks using radiative kernels, J. Climate, 21, 3504-3520, https://doi.org/10.1175/2007jcli2110.1,

690   2008.

691 Stephens, G. L., Vane, D. G., Boain, R. J., Mace, G. G., Sassen, K., Wang, Z., Illingworth, A. J., O'connor,

692   E. J., Rossow, W. B., Durden, S. L., Miller, S. D., Austin, R. T., Benedetti, A., and Mitrescu, C. A.:

693   The CloudSat Mission and the A-Train, Bull. Amer. Meteor. Soc., 83, 1771–1790,

694   https://doi.org/10.1175/BAMS-83-12-1771, 2002.

695 Stevens, B., Brogniez, H., Kiemle, C., Lacour, J.-L., Crevoisier, C., and Kiliani, J.: Structure and

696   dynamical influence of water vapor in the lower tropical troposphere, Surv. Geophys., 38, 1371-1397,

697   https://doi.org/10.1007/s10712-017-9420-8, 2017.

698 Su, H. and Jiang, J. H.: Tropical clouds and circulation changes during the 2006/07 and 2009/10 El Niños,

699   J. Climate, 26, 399-413, https://doi.org/10.1175/JCLI-D-12-00152.1, 2013.

700 Sun, M., Cess, R. D., and Doelling, D. R.: Interpretation of cloud structure anomalies over the tropical

701   Pacific during the 1997/98 El Niño, J. Geophys. Res.-Atmos., 117,

702   https://doi.org/10.1029/2011JD015861, 2012.

703 Susskind, J., Blaisdell, J. M., and Iredell, L.: Improved methodology for surface and atmospheric

704   soundings, error estimates, and quality control procedures: the atmospheric infrared sounder science

705   team version-6 retrieval algorithm, J. Appl. Remote Sens., 8, 084994,

https://doi.org/10.1117/1.Jrs.8.084994, 2014.

Ssenyunzi, R. C., Oruru, B., D'ujanga, F. M., Realini, E., Barindelli, S., Tagliaferro, G., von Engeln, A.,
and van de Giesen, N.: Performance of ERA5 data in retrieving precipitable water vapour over East
African tropical region, Adv. Space Res., 65, 1877-1893,
https://doi.org/https://doi.org/10.1016/j.asr.2020.02.003, 2020.

Takahashi, H., Su, H., Jiang, J. H., Luo, Z. J., Xie, S.-P., and Hafner, J.: Tropical water vapor variations
during the 2006-2007 and 2009-2010 El Niños: Satellite observation and GFDL AM2.1 simulation, J.
Geophys. Res.-Atmos., 118, 8910-8920, https://doi.org/10.1002/jgrd.50684, 2013.

Takemoto, M. and Tanaka, H. L.: Intensities of Hadley, Walker, and monsoon circulations compared in the
upper and lower troposphere, J. Korean Meteor. Soc., 43(3), 239-251, 2007.

Tanaka, H. L., Ishizaki, N., and Kitoh, A.: Trend and interannual variability of Walker, monsoon and
Hadley circulations defined by velocity potential in the upper troposphere, Tellus A, 56, 250-269,
https://doi.org/10.1111/j.1600-0870.2004.00049.x, 2004.

Tanaka, H. L., Ishizaki, N., and Nohara, D.: Intercomparison of the intensities and trends of Hadley,
Walker and monsoon circulations in the global warming projections, SOLA, 1, 77-80,
https://doi.org/10.2151/sola.2005-021, 2005.

Viswanadham, Y.: The relationship between total precipitable water and surface dew point, J. Appl.
Meteorol. Climatol., 20, 3-8, https://doi.org/10.1175/1520-0450(1981)020<0003:TRBTPW>2.0.CO;2,
1981.

Wang, C.: Atmospheric circulation cells associated with the El Niño Southern Oscillation, J. Climate, 15,
399-419, https://doi.org/10.1175/1520-0442(2002)015<0399:ACCAWT>2.0.CO;2, 2002.

Wang, J., Zeng, N., Wang, M., Jiang, F., Chen, J., Friedlingstein, P., Jain, A. K., Jiang, Z., Ju, W., Lienert,

728   S., Nabel, J., Sitch, S., Viovy, N., Wang, H., and Wiltshire, A. J.: Contrasting interannual atmospheric

729   CO_2 variabilities and their terrestrial mechanisms for two types of El Niños, Atmos. Chem. Phys.,

730   18, 10333-10345, https://doi.org/10.5194/acp-18-10333-2018, 2018.

731   Wang, S., Xu, T., Nie, W., Jiang, C., Yang, Y., Fang, Z., Li, M., and Zhang, Z.: Evaluation of precipitable

732   water vapor from five reanalysis products with ground-based GNSS observations, Remote Sens., 12,

733   https://doi.org/10.3390/rs12111817, 2020.

734   Wang, X., Jiang, X., Yang, S., and Li, Y.: Different impacts of the two types of El Niño on Asian summer

735   monsoon onset, Environ. Res. Lett., 8, https://doi.org/10.1088/1748-9326/8/4/044053, 2013.

736   Weng, H., Behera, S. K., and Yamagata, T.: Anomalous winter climate conditions in the Pacific rim during

737   recent El Niño Modoki and El Niño events, Climate Dyn., 32, 663-674,

738   https://doi.org/10.1007/s00382-008-0394-6, 2008.

739   Winker, D. M., Hunt, W. H., and McGill, M. J.: Initial performance assessment of CALIOP, Geophys. Res.

740   Lett., 34, https://doi.org/10.1029/2007gl030135, 2007.

741   Xu, K., Tam, C.-Y., Zhu, C., Liu, B., and Wang, W.: CMIP5 projections of two types of El Niño and their

742   related tropical precipitation in the twenty-First century, J. Climate, 30, 849-864,

743   https://doi.org/10.1175/jcli-d-16-0413.1, 2017.

744   Yan, X., Konopka, P., Ploeger, F., Tao, M., Müller, R., Santee, M. L., Bian, J., and Riese, M.: El Niño

745   southern oscillation influence on the Asian summer monsoon anticyclone, Atmos. Chem. Phys., 18,

746   8079-8096, https://doi.org/10.5194/acp-18-8079-2018, 2018.

747   Ye, H., Fetzer, E. J., Bromwich, D. H., Fishbein, E. F., Olsen, E. T., Granger, S. L., Lee, S.-Y., Chen, L.,

748   and Lambrigtsen, B. H.: Atmospheric total precipitable water from AIRS and ECMWF during

749   Antarctic summer, Geophys. Res. Lett., 34, https://doi.org/10.1029/2006gl028547, 2007.

750   Yeh, S.-W., Kug, J.-S., Dewitte, B., Kwon, M.-H., Kirtman, B. P., and Jin, F.-F.: El Nino in a changing

751   climate, Nature, 461, 511-514, https://doi.org/10.1038/nature08316, 2009.

752   Yeh, S.-W., Kug, J.-S., and An, S.-I.: Recent progress on two types of El Niño: Observations, dynamics,

753   and future changes, Asia-Pac. J. Atmos. Sci., 50, 69-81, https://doi.org/10.1007/s13143-014-0028-3,

754   2014.

755   Yu, J.-Y. and Kao, H.-Y.: Contrasting eastern-Pacific and central-Pacific types of ENSO, J. Climate, 22,

756   615-632, https://doi.org/10.1175/2008jcli2309.1, 2009.

757   Zhao, P., Yang, S., and Yu, R.: Long-term changes in rainfall over eastern China and large-scale

758   atmospheric circulation associated with recent global warming, J. Climate, 23, 1544-1562,

759   https://doi.org/10.1175/2009jcli2660.1, 2010.
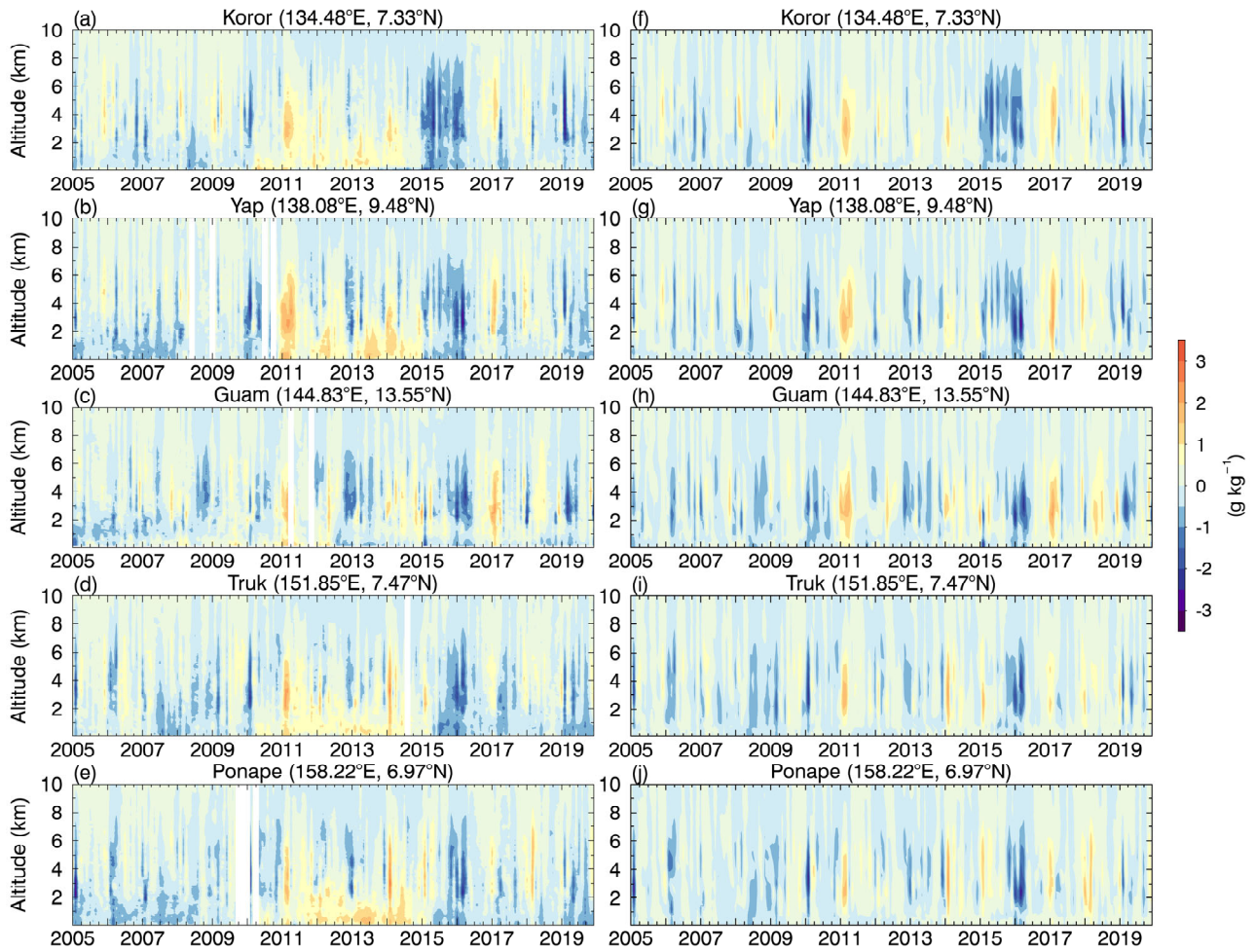
Figure 1. Specific humidity anomaly between January 2005 and December 2019 derived from (left) radiosonde observations and (right) ERA5 reanalysis data at (a, f) Koror, (b, g) Yap, (c, h) Guam, (d, i) Truk and (e, j) Ponape.
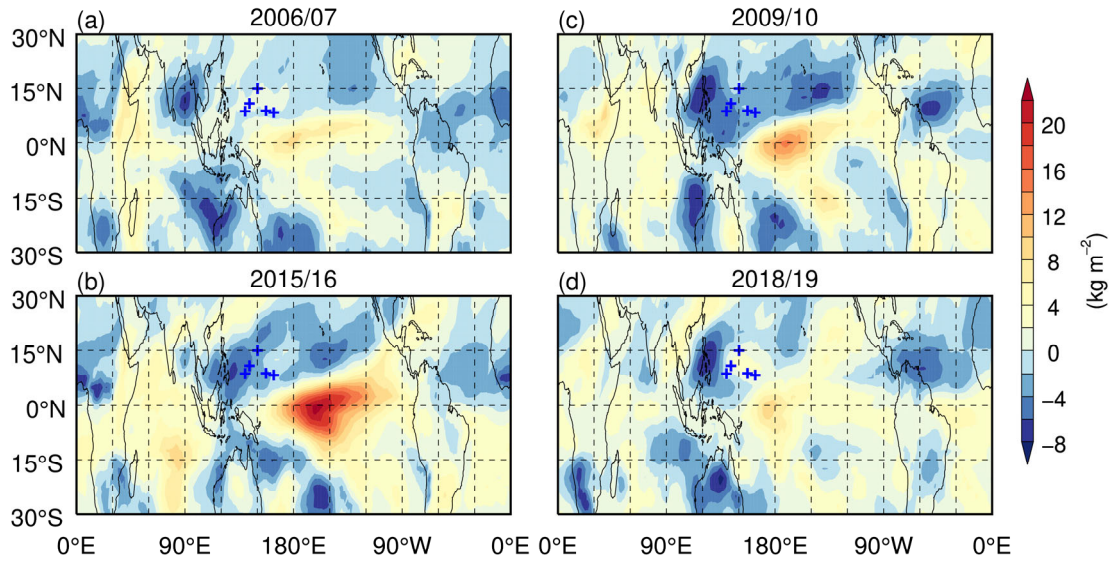
Figure 2. CWV anomalies averaged in (a) 2006/07, (b) 2015/16, (c) 2009/10 and (d) 2018/19 winters derived from ERA5 reanalysis data. The blue plus denotes the five radiosonde stations. The four El Niño events are classified into (left) EP El Niño and (right) CP El Niño.
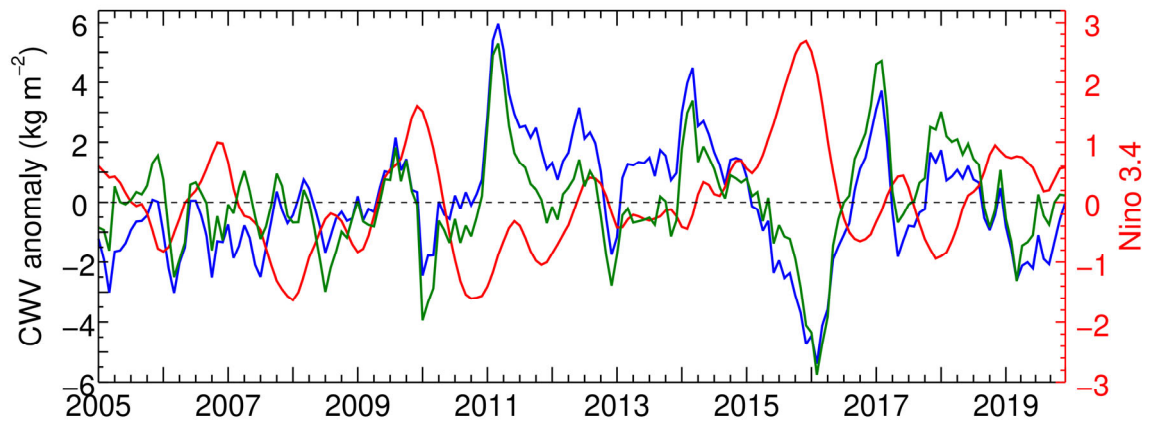
Figure 3. Time series of (red) ONI index and monthly mean CWV anomalies derived from (blue) radiosonde observation and (green) reanalysis data at five radiosonde stations.
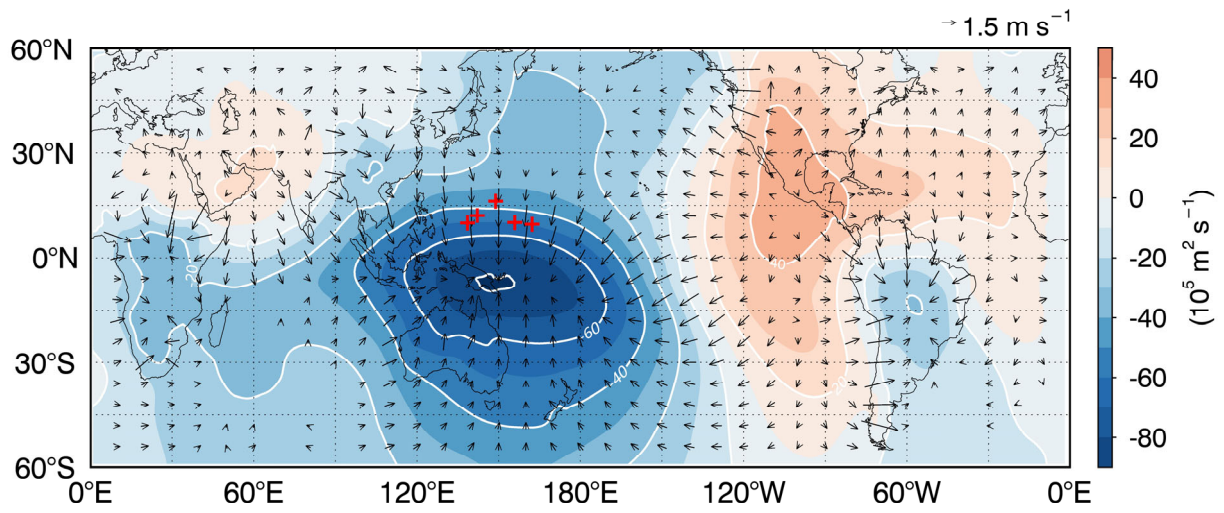
Figure 4. Climatic means of (shading) velocity potential and (arrow) divergent wind fields at 850 hPa in

DJF derived from reanalysis data during 2005-2019. The red plus denotes the five radiosonde stations.
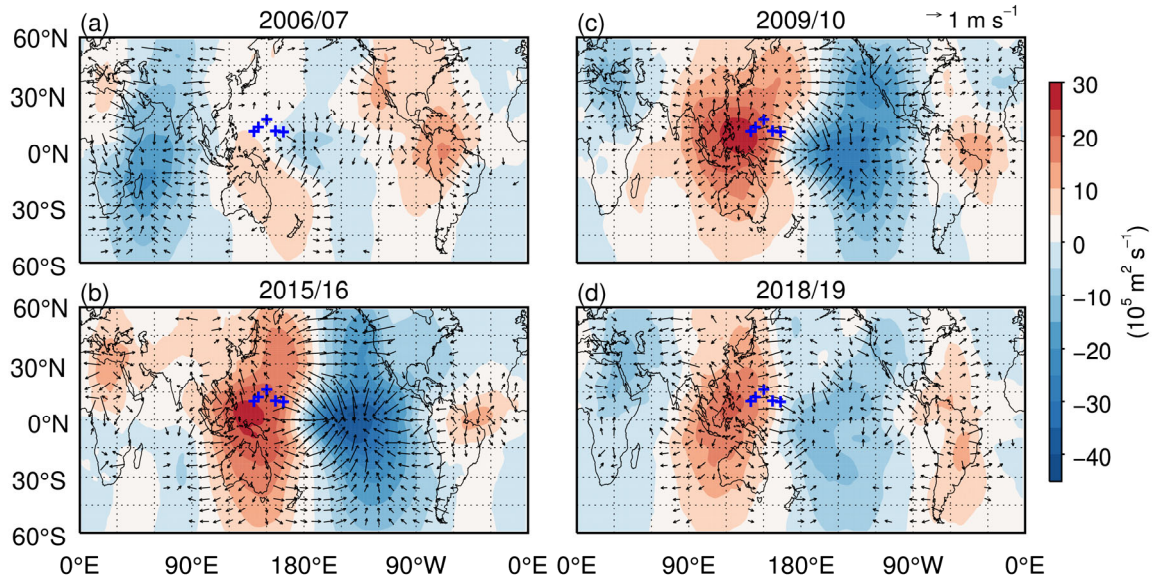
Figure 5. Anomalies of (shading) velocity potential and (arrow) divergent wind at 850 hPa in winters of (a) 2006/07, (b) 2015/16, (c) 2009/10 and (d) 2018/19. The blue plus denotes the five radiosonde stations.
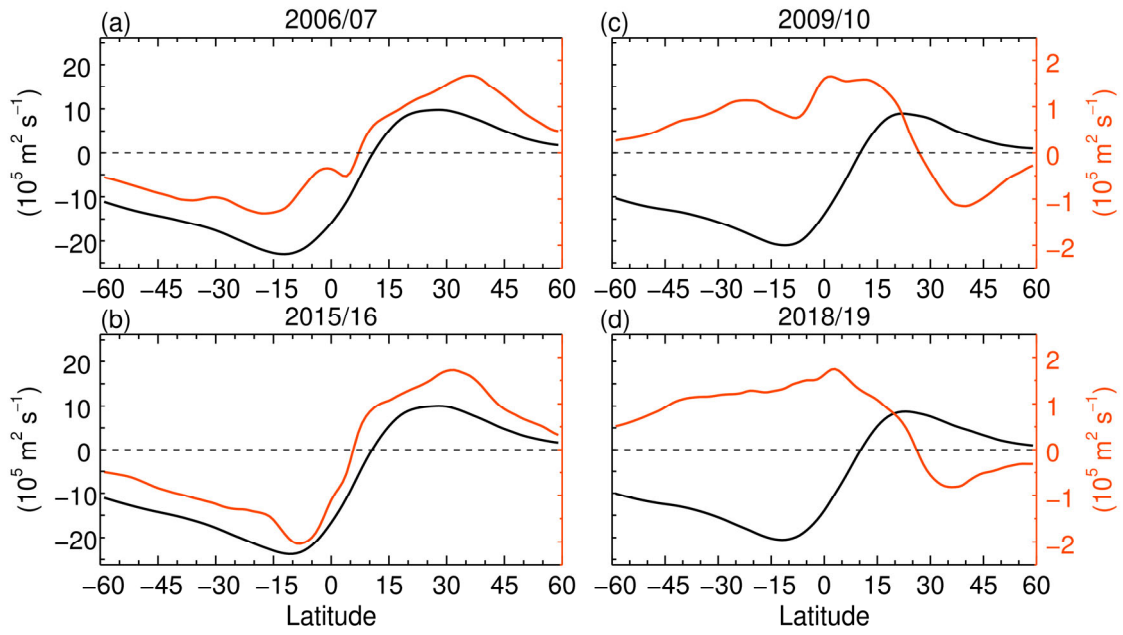
Figure 6. (Black)Velocity potential and (orange) anomaly index of Hadley circulation at 850 hPa derived

from reanalysis data in (a) 2006/07, (b) 2015/16, (c) 2009/10 and (d) 2018/19 winters.
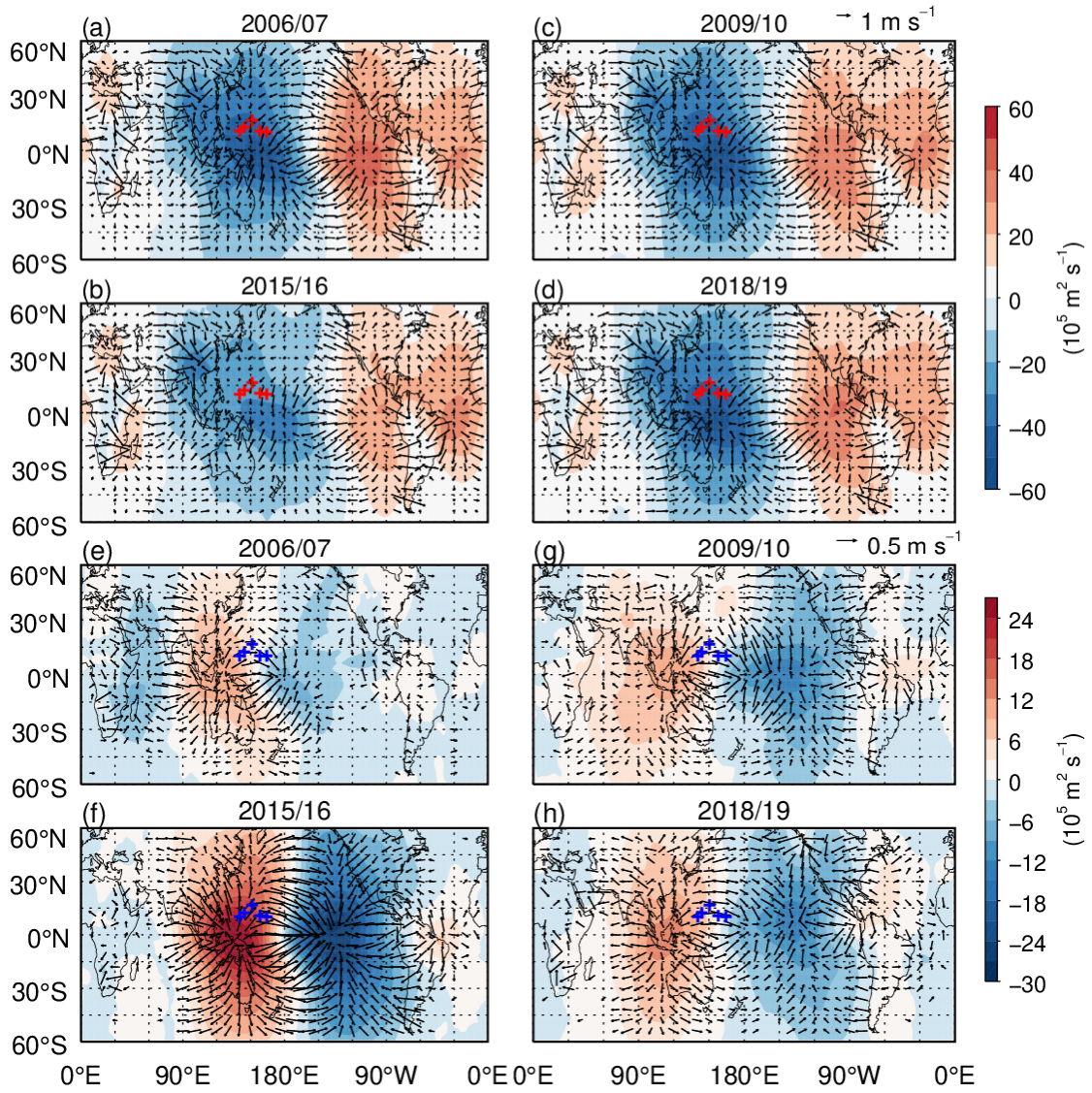
Figure 7. (shading) Velocity potential and (arrow) divergent wind of Walker circulation and their anomalies at 850 hPa in (a, e) 2006/07, (b, f) 2015/16, (c, g) 2009/10 and (d, h) 2018/19 winters. Figure 7 (a-d) denotes the velocity potential and divergent wind, and Figure 7 (e-h) denotes their anomalies. The red and blue plus denotes the five radiosonde stations.
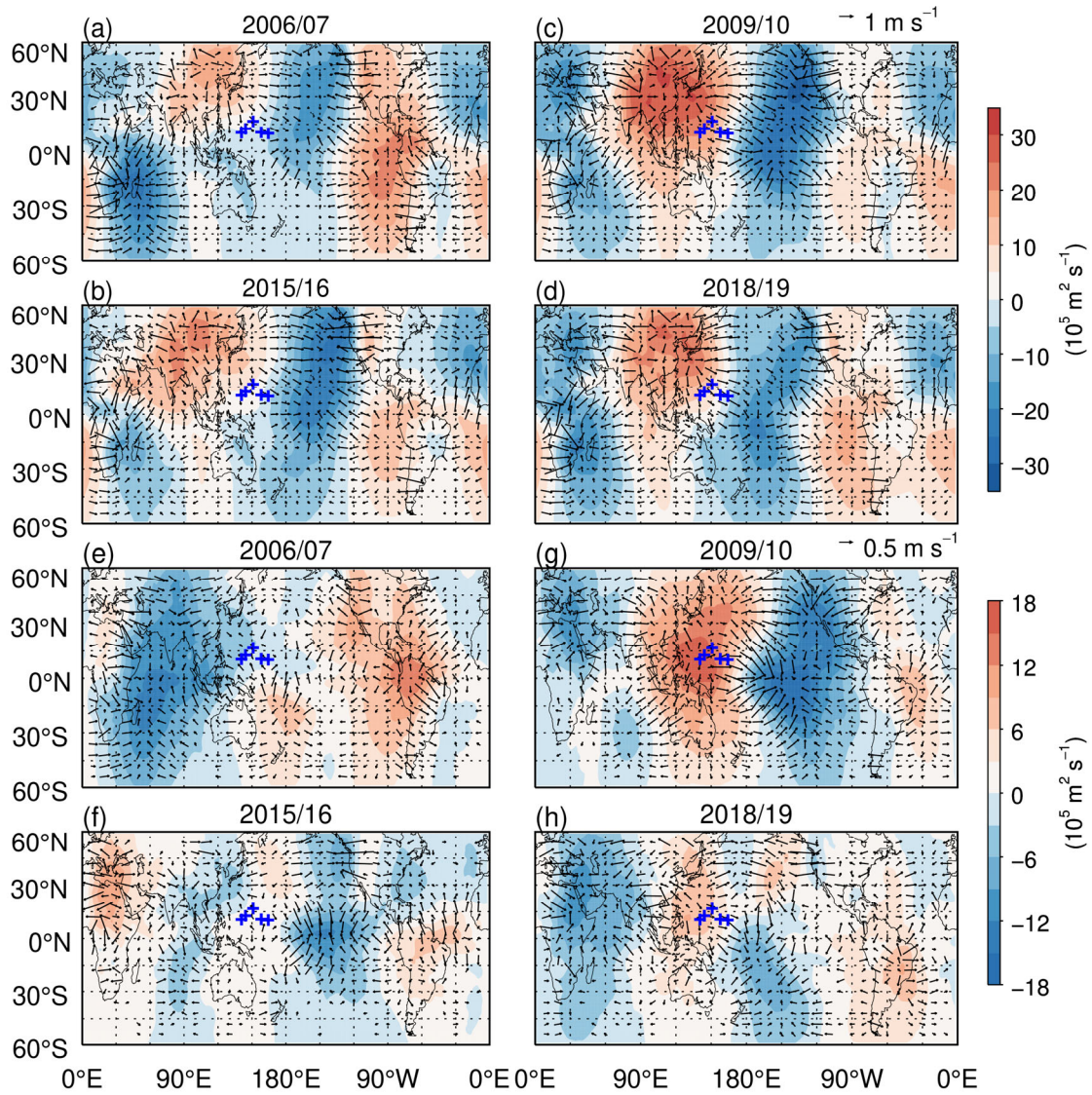
Figure 8. (shading) Velocity potential and (arrow) divergent wind of monsoon circulation and their anomalies at 850 hPa in (a, e) 2006/07, (b, f) 2015/16, (c, g) 2009/10 and (d, h) 2018/19 winters. Figure 8(a-d) denotes the velocity potential and divergent wind, and Figure 8(e-h) denotes their anomalies. The blue plus denotes the five radiosonde stations.
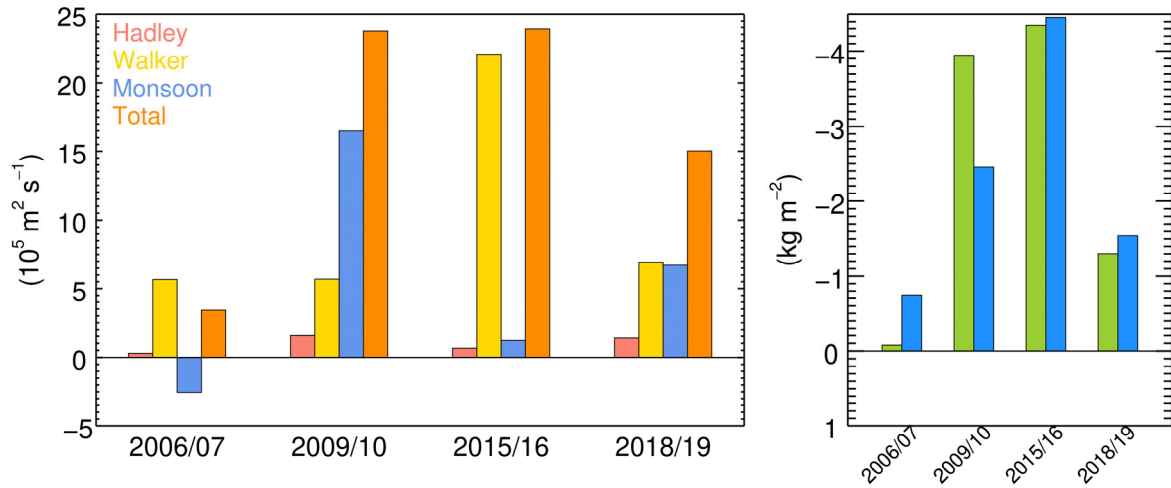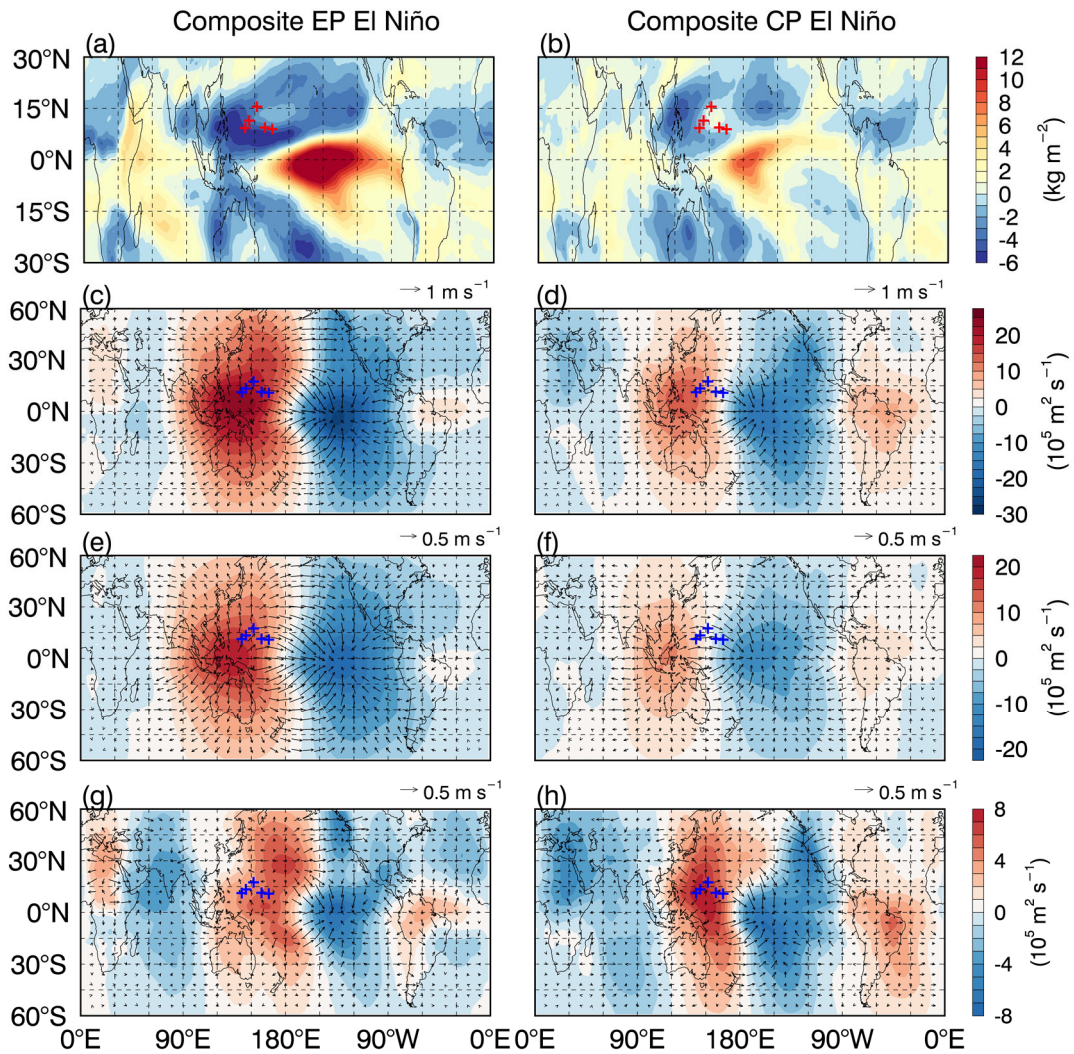
Figure 9. (Left) Indices of (red) Hadley, (yellow) Walker, (blue) monsoon and (orange) total circulation anomalies and (right) CWV anomalies derived from (azure) radiosonde and (green) reanalysis data at five radiosonde stations in four El Niño winters.

Figure 10. Anomalies of (a, b) CWV and velocity potential and divergent wind at 850 hPa in (c, d) total, (e, f) Walker and (g, h) monsoon circulations for composite EP and CP El Niños derived from reanalysis data. The left and right columns correspond to the composite EP and CP El Niños, respectively. The shading and arrow in Fig. 10 (c-h) denote the velocity potential and divergent wind anomalies, respectively. The red and blue plus denotes the five radiosonde stations.
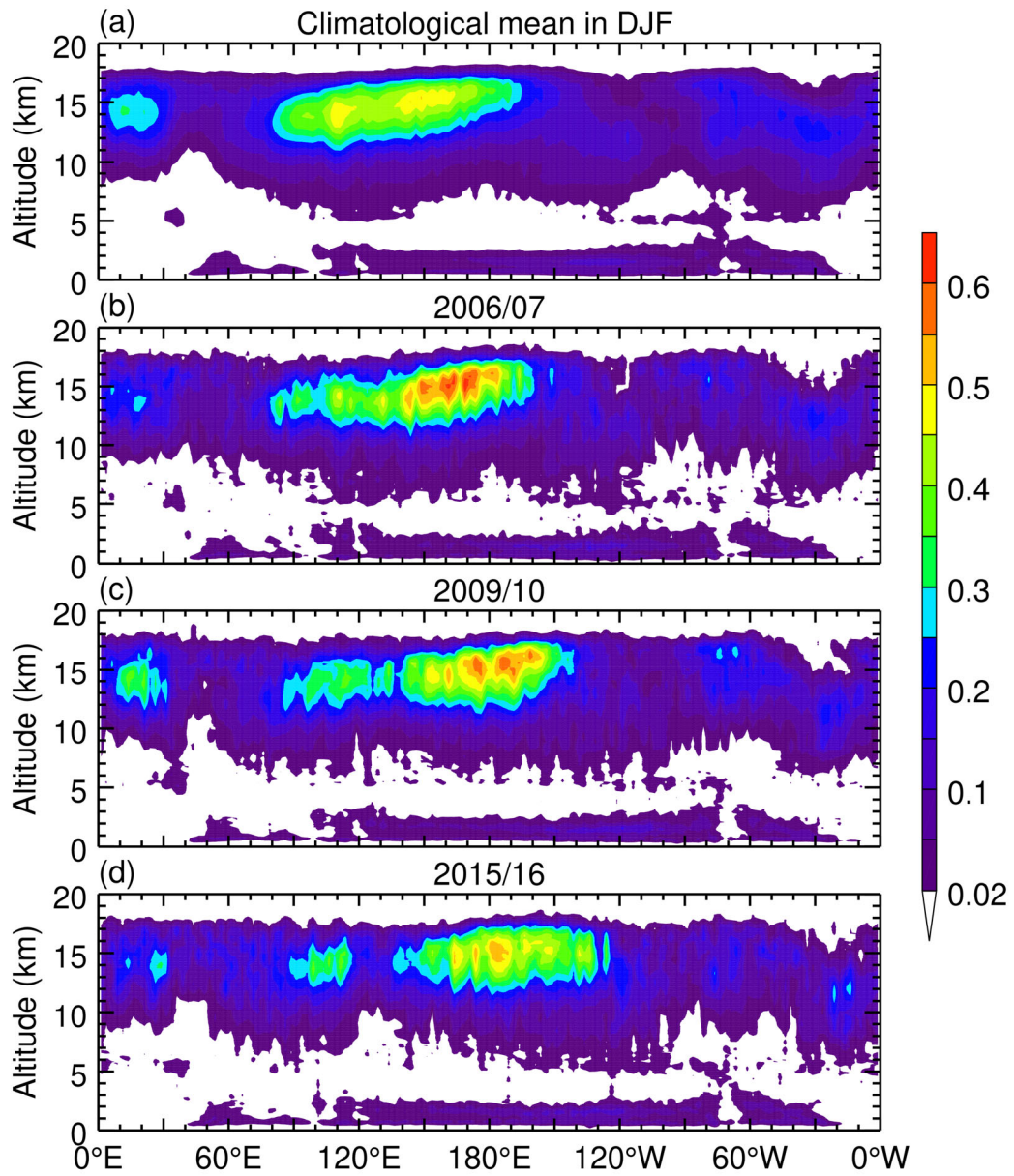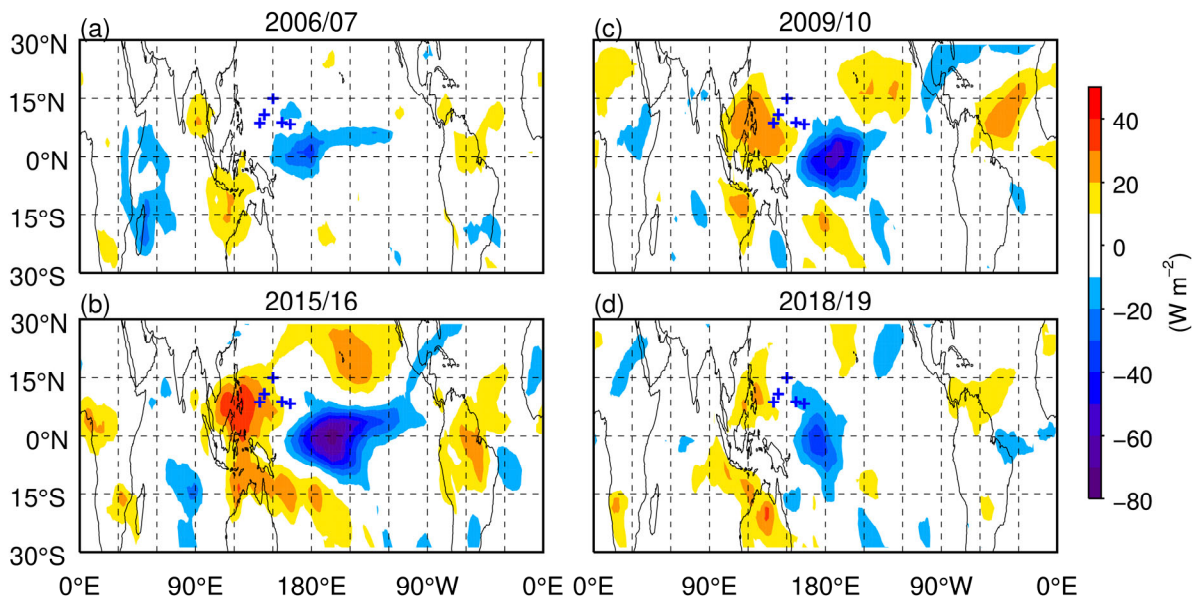
Figure 11. Distribution of cloud occurrence between 0°N and 15°N in (a) all winters, and (b) 2006/07, (c)

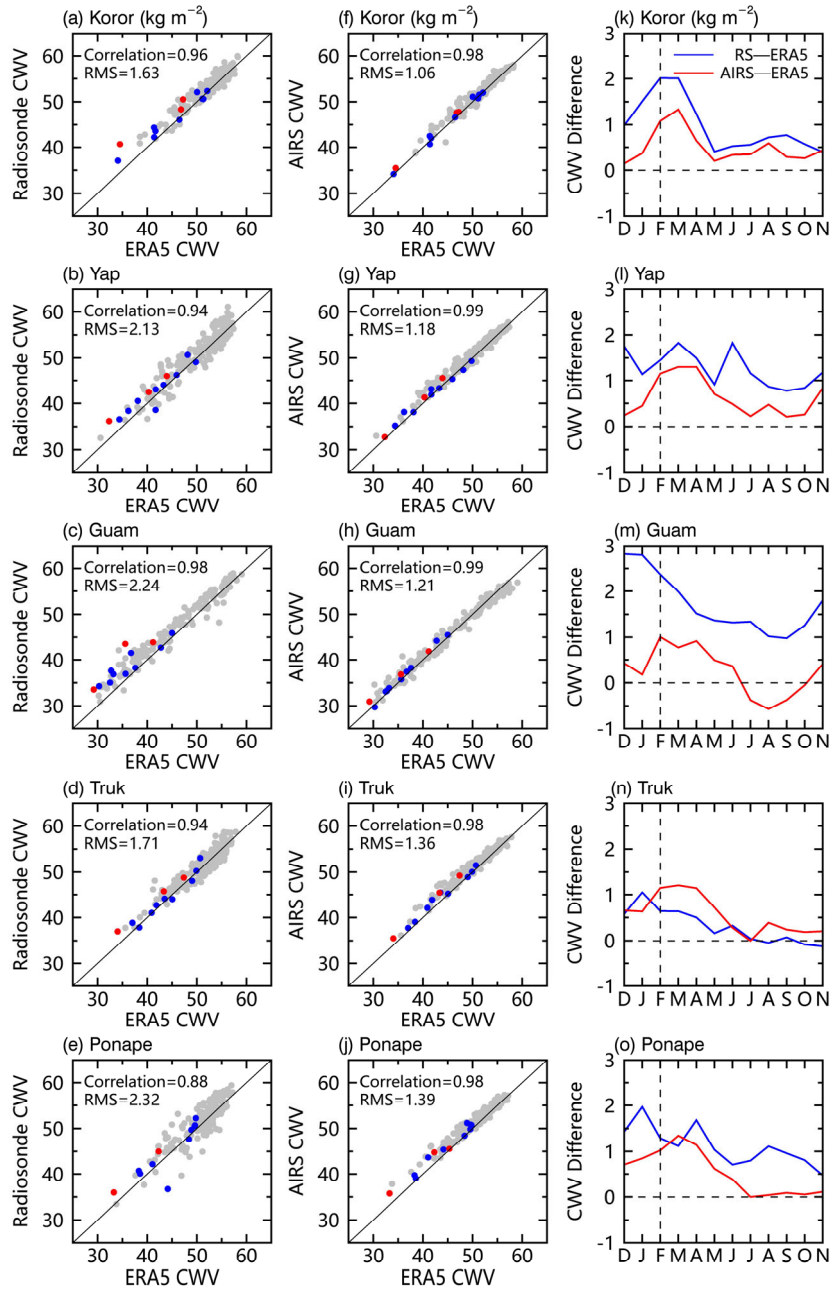2009/10 and (d) 2015/16 winters derived from CALIPSO during June 2006 to December 2016.

Figure 12. OLR anomalies averaged in (a) 2006/07, (b) 2015/16, (c) 2009/10 and (d) 2018/19 winters.

The blue plus denotes the five radiosonde stations.

Figure 13. Scatterplots of monthly mean CWV in winter derived from (a-e) radiosonde and (f-j) AIRS observations against corresponding CWV from ERA5 reanalysis and (k-o) climatic mean CWV difference (blue lines) between radiosonde and ERA5 reanalysis data and (red lines) between AIRS and ERA5 reanalysis data at five stations during 2005-2019. In Fig. (a-j), the red, blue and gray dots denote the CWV values in the 2009/10 winter, the 2006/2007, 2015/2016 and 2018/2019 winters, and the other winters, respectively.